Impacts of salinity variation on the mixed-layer processes and sea surface temperature in the Kuroshio-Oyashio confluence region

Shoichiro Kido[1]
Masami Nonaka[1]
Youichi Tanimoto[1,2]

(4th revision)

1: Application Laboratory (APL), Research Institute for Value-Added-Information Generation (VAiG), Japan Agency for Marine-Earth Science and Technology (JAMSTEC), Yokohama, Japan

2: Faculty of Environmental Earth Science, Hokkaido University, Sapporo, Japan

Key points:

1. Coherent temperature and salinity variations are identified in the Kuroshio-Oyashio confluence region during boreal winter to spring
2. The dynamical stability of the Kuroshio Extension is the key factor responsible for these temperature and salinity variations
3. Changes in density field associated with salinity anomalies significantly affect the strength of vertical mixing and sea surface temperature

Abstract:

In this study, salinity variations in the Kuroshio–Oyashio confluence region (KOCR) are examined through analyses of observational datasets and an ocean reanalysis product, and their potential impacts on sea surface temperature are assessed by sensitivity experiments using a one-dimensional mixed layer model (1-D ML model). We have detected prominent covariations in near surface temperature and salinity in the KOCR during the boreal winter to spring. Further investigation revealed that such covariations are closely related to the dynamical stability of the Kuroshio Extension (KE), and anomalous warming and saltening (cooling and freshening) are observed in the KOCR when the upstream of the KE is in an unstable (a stable) state. It is found that modulation heat and freshwater transport by mesoscale eddies and large-scale current anomalies are closely related to such observed variation. Then, we have quantitatively estimated the impacts of these salinity variations on local density by a detailed decomposition of total anomaly fields. Although the total density anomalies are dominated by contributions from temperature, the salinity contribution has sizable magnitude especially in the northern part of the KOCR, where the background temperature is low and the dependence of density on temperature variations is weak. To further quantify the impact of salinity anomalies, we conducted a series of sensitivity experiments utilizing the 1-D ML model. The results from these experiments revealed that salinity anomalies significantly alter the strength of vertical mixing and eventually lead to differences in sea surface temperature of approximately 1.0 °C.

(245 words < 250 words)

Plain Language summary:

The Kuroshio–Oyashio confluence region (KOCR) in the western North Pacific Ocean undergoes well-defined low-frequency variation on interannual to decadal time scales, and play a pivotal role in the climate variability of the North Pacific. Although significant progress has been made in understanding the dynamical and thermodynamical characteristics of the KOCR variations, less attention has been paid to salinity variability. With the variation in the density of seawater, salinity can potentially exert significant effects on various physical processes in the upper ocean. Therefore, it is important to properly describe its features and assess its possible impacts. In pursuit of these objectives, herein we investigate salinity variations in the KOCR and its possible impacts through analysis of observational datasets and sensitivity experiments using a simplified model. We found that the upper ocean temperature and salinity in the KOCR exhibit distinct covariation during boreal winter, and they are primarily caused by modulations of ocean circulation in the same region. A detailed decomposition of density anomalies and numerical experiments demonstrated that these salinity anomalies significantly affect the strength of vertical mixing and sea surface temperature, suggesting that salinity has a potential to play an active role in low-frequency variations of the KOCR.

(199 words < 200 words)

1. Introduction

The upper ocean circulation in the western North Pacific is characterized by two remarkable western boundary currents, namely the Kuroshio and Oyashio, which constitute the subtropical and subarctic gyres, respectively (Fig. 1a) (Qiu, 2002; Yasuda, 2003). Warm and saline subtropical water is transported poleward by the Kuroshio, whereas cold and fresh water from the subpolar region is advected equatorward by the Oyashio. After separating from the coast of Japan, these western boundary currents and associated water masses meet together to form the Kuroshio–Oyashio confluence region (KOCR). Due to the marked differences in the physical properties of these water masses, the hydrographic structures of the KOCR are far from uniform and many complicated but intriguing features, such as sharp sea surface temperature (SST) and salinity (SSS) fronts (Figs. 1b, c), vigorous submesoscale/mesoscale eddies, as well as abrupt changes in vertical stratification (Fig. 1d) are observed (Kida et al., 2015; Roden, 1972; I. Yasuda, 2003; Yuan & Talley, 1996).

The oceanic variables (e.g. temperature, salinity, sea surface height (SSH), and current fields) in the KOCR undergo significant variations on various time scales, and interannual to decadal variability in surface and subsurface temperature is especially strong near the climatological fronts (Figs. 1e, f) (Nakamura et al., 1997; Nakamura & Kazmin, 2003; Nonaka et al., 2006). As SST fronts in the KOCR affect the baroclinicity of the lower troposphere and anchor the latitude of the extratropical storm tracks (Nakamura et al., 2004), changes in the KOCR SST not only significantly modulate the local atmospheric conditions but also exert substantial effects on large-scale atmospheric circulation (Frankignoul et al., 2011; Kwon et al., 2010; Ma et al., 2015; Smirnov et al., 2015; Taguchi et al., 2012). The KOCR is also known as a key region for water mass formation. Reflecting the intricate hydrographic structures, strong horizontal gradients of the mixed layer depth (MLD) can be seen in the KOCR (Fig. 1d), and they also experience large low-frequency variations as well as other oceanic parameters (Fig. 1f) (Oka et al., 2012; Suga et al., 2004). The inhomogeneous distribution of the MLD in the KOCR is conducive to the formation of mode waters, which are characterized by vertically uniform water properties and believed to play an important role in long-term climate variability and biogeochemical processes. Indeed, various types of mode water are formed in the vicinity of the KOCR, such as the subtropical mode water (Masuzawa, 1969), central mode water (Suga et al., 1997), and transition region mode water (Saito et al., 2007), and their variations are closely linked to the variability of the KOCR (see review by Oka & Qiu, 2012). For these reasons, a comprehensive description and understanding of oceanic variations in the KOCR are of particular interests from various perspectives.

Thanks to the progress of observational platforms and numerical ocean models in recent decades, significant advances have been made in understanding the driving mechanisms of oceanic variations in the KOCR and other western boundary current regions (Kelly et al., 2010; Kwon et al., 2010). In particular, many studies have attempted to clarify the processes that contribute to the generation of SST anomalies in the KOCR, which is a key variable for air–sea interactions (Pak et al., 2017; Qiu, 2000; Qiu & Kelly, 1993; Vivier et al., 2002). Unlike majority of the extratropical ocean, SST variations in the KOCR are predominantly regulated by ocean dynamical process, rather than being passively forced by the atmosphere (Sugimoto & Hanawa, 2011; Tanimoto et al., 2003). The dynamical and thermodynamical processes responsible for these SST anomalies are governed by multiple factors, with both deterministic forcing and intrinsic variability contributing to their variations. On the one hand, upwelling/downwelling Rossby waves excited by the large-scale wind stress curl anomalies in the central to eastern part of the North Pacific alter the intensity of the inertial jet, the latitude of the subtropical-subarctic gyre, and the thermocline depth of the KOCR, giving rise to significant SST anomalies (Kwon & Deser, 2007; Nonaka et al., 2006, 2008; Schneider et al., 2002; Seager et al., 2001). These changes in large-scale ocean circulation also affect the strength of mesoscale eddy activity (Qiu & Chen, 2005, 2010) and associated heat transport (Itoh & Yasuda, 2010; Sasaki & Minobe, 2015; Sugimoto et al., 2014). Furthermore, changes in the Ekman transport associated with anomalous wind forcing may also contribute to the generation SST anomalies (Nakamura & Kazmin, 2003; Yasuda & Hanawa, 1997). In addition to such deterministic forcing, internal variability arising from nonlinearities in the western boundary current system (Pierini, 2006; Pierini et al., 2009; Taguchi et al., 2007) also play an important role in the low-frequency variability of the KOCR, particularly on the frontal scale (Nonaka et al., 2012, 2016, 2020; Taguchi et al., 2007). Superimpositions of these two factors (i.e. external forcing and intrinsic variability) and mutual interactions between them control the observed variability in the KOCR (Qiu & Chen, 2010; Taguchi et al., 2007, 2010).

Although our knowledge of the upper ocean dynamics and thermodynamics of the KOCR has been considerably enhanced by a large body of previous literature, less is known about salinity, which also exhibits pronounced low-frequency variation (Fig. 1g). This is attributed to the paucity of in-situ salinity observations and difficulty in accurately simulating salinity in numerical ocean models; however, the deployment of Argo profiling floats in the 2000s have rapidly changed this situation. Newly available datasets based on the Argo profiles have enabled the identification of long-term trends and low-frequency variability in the surface and subsurface salinity in the western North Pacific (Geng et al., 2018; Kitamura et al., 2016; Nan et al., 2015; Yan et al., 2013). The governing mechanisms of such salinity variations have also been explored by means of a salinity budget analysis (Geng et al., 2018; Kitamura et al., 2016; Nagano et al., 2014; Sugimoto et al., 2013), but the relative importance of the freshwater flux and advective processes has not been conclusively established in these studies. Such discrepancies could be due to insufficient spatiotemporal resolutions of the observational and reanalysis products used in these studies; therefore, further quantitative assessments based on more comprehensive observations and/or high-resolution ocean models are required. In addition, the possible impacts of these salinity variations on density structures and the evolution of SST are yet to be assessed, although salinity has been shown to play active roles in the tropical climate variability, such as the El Niño-Southern Oscillation (ENSO) (Hasson et al., 2013; Vialard & Delecluse, 1998; Zhu et al., 2015) and the Indian Ocean Dipole (Kido et al., 2019a, 2019b; Kido & Tozuka, 2017; Li et al., 2018; Zhang et al., 2016). Given that seawater density becomes more dependent on salinity than temperature in lower temperature conditions (Gill, 1982), salinity variations in the KOCR have the potential to affect upper ocean processes and related parameters.

To address these issues, we investigate the features and mechanisms of salinity variations in the KOCR through an analysis of the observational datasets and an eddy-resolving ocean reanalysis product. In addition, the potential impacts of salinity upon the mixed layer processes are further examined by means of sensitivity experiments using a one-dimensional mixed layer (1-D ML) model. The remainder of this paper is organized as follows. In Section 2, we outline the observational datasets and ocean reanalysis product used in this study. We also briefly describe the 1-D ML model adopted to assess the salinity impacts. The main features of salinity variations in the KOCR and their underlying mechanisms are discussed in Section 3. Then, in Section 4, we assess the impacts on the density structure and SST through a decomposition of the density anomalies and sensitivity experiments using the 1-D ML model. A summary and discussion are presented in Section 5.

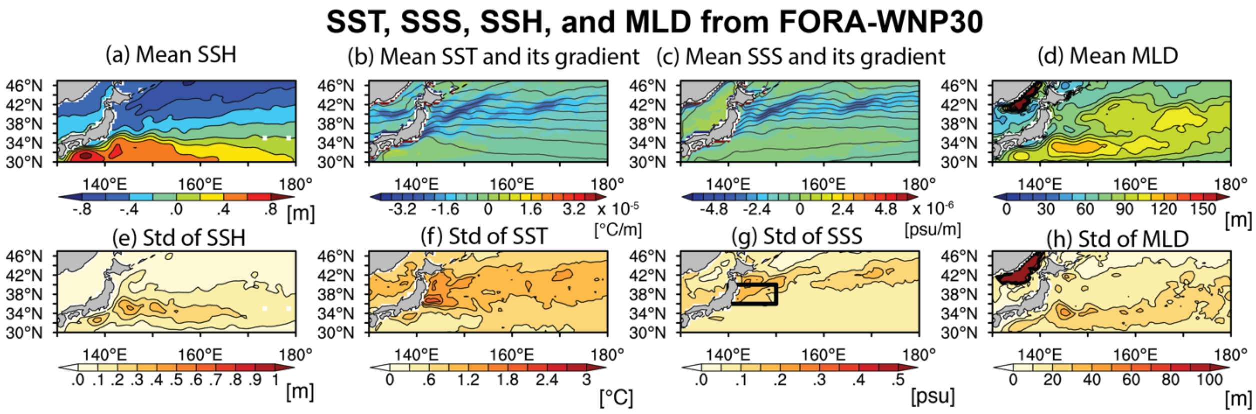

Figure 1. Long-term mean climatology of annual mean: (a) sea surface height (SSH: in m); (b) sea surface temperature (SST: in °C) and its meridional gradient (color); (c) sea surface salinity (SSS: in psu) its meridional gradient (color); and (d) mixed layer depth (MLD in m) derived from the Four-Dimensional Variational Ocean Reanalysis for the Western North Pacific over 30 Years (FORA-WNP30). The contour intervals in (a), (b), (c), and (d) are 0.1, 4×10^{-6}, 6×10^{-7}, and 10, respectively, and the MLD is defined as the depth at which the potential density increases by 0.125 kg m^{-3} from the sea surface. (e)-(h): As in (a)-(d), but with the standard deviation of interannual anomalies (with monthly climatology removed and a 3-month running mean is applied to anomaly fields). Contour intervals in (e), (f), (g), and (h) are 0.1, 0.3, 0.05, and 10, respectively.

2. Data and method

2.1 Observational data

In the present study, we analyze the Argo-based gridded temperature and salinity field provided by the Scripps Institution of Oceanography (Roemmich & Gilson, 2009; hereinafter RG09), which has a horizontal resolution of 1° longitude × 1° latitude and 58 vertical levels, 25 of which are in the upper 300 m. Monthly data from January 2004 to December 2019 is used in this study. Prior to the analysis, a linear interpolation for 5-m intervals is applied onto the vertical profiles in temperature and salinity. To check the robustness of results, we also adopted the Grid Point Value of the Monthly Objective Analysis (MOAA-GPV) (Hosoda et al., 2008).

To complement the limited spatiotemporal coverage of the Argo data and extend the analysis period to 1990s, we use the Four-Dimensional Variational Ocean Reanalysis for the Western North Pacific over 30 Years (FORA-WNP30). The FORA-WNP30 is an eddy-resolving ocean reanalysis product developed by the Meteorological Research Institute of the Japan Meteorological Agency (MRI-JMA) and the Japan Agency for Marine-Earth Science and Technology (JAMSTEC) (Usui et al., 2017). The core ocean model employed for the FORA-WNP 30 is the MRI Community Ocean model version 2.4 (Tsujino et al., 2006), which is configured for the western North Pacific (117°E to 160°W, 15°N to 60°N). The model has a spatially varying horizontal resolution, with 1/10° from 117°E to 160°E (from 15°N to 50°N) and 1/6° from 160°E to 160°W (from 50°N to 60°N) in the zonal (meridional) direction, and 54 vertical levels, with increasing grid spacing from 1 m at the surface to 600 m at the bottom (set to 6300 m depth). Atmospheric forcing of the model is derived from the JRA-55 atmospheric reanalysis product (Kobayashi et al., 2015) with a daily resolution. The FORA-WNP30 assimilates various observational data, such as in situ temperature and salinity profiles (including

Argo profiles), gridded sea surface height (SSH), SST, and sea ice concentrations derived from satellites using the four-dimensional variational scheme called the MOVE-4DVAR (Usui et al., 2015). In addition to temperature and salinity, we analyze the SSH and horizontal velocity to explore the related physical processes. Surface and subsurface oceanic fields of the FORA-WNP30 have been validated against various types of in-situ and satellite observation (Usui et al. 2017) and realistically reproduce the observed seasonal features, such as the location of the ocean fronts (Kida et al., 2015) and the wintertime ML distribution (Suga et al., 2004) in the western North Pacific (for example, see their Fig. 12). As in the MOAA-GPV, all three-dimensional data were linearly interpolated into 5-m intervals in the vertical direction. The FORA-WNP30 data are available for between January 1982 and December 2014 as a daily average, but we focus on the period from 1991 to 2013, as the surface atmospheric flux product employed in this study (J-OFURO3; for a description, see below) is not available for other periods. We note that the results are qualitatively similar even if we use outputs from the entire period.

In addition to the gridded Argo data and FORA-WNP30, the surface variables (net heat surface fluxes, including shortwave and longwave radiation, sensible and latent heat fluxes, and freshwater flux) from the Japanese Ocean Flux Datasets with Use of Remote Sensing Observation (J-OFURO3) (Tomita et al., 2019) at a horizontal resolution of 0.25° and available from 1991 to 2013 are employed to examine the possible contribution of atmospheric forcing.

2.2 1-D model experiment

To quantitatively assess the potential impact of salinity anomalies on the mixed layer formation and evolution of SST, we need to explicitly deal with the vertical mixing operating within the upper ocean. Given the strong horizontal currents and associated large heat and salt transports in this region (Qiu & Kelly, 1993; Vivier et al., 2002), here we adopt a 1-D ML model that can implicitly incorporate advective effects through prescribed forcing (Kido & Tozuka, 2017) and conducted a series of sensitivity experiments. The 1-D ML model employed in this study is a level-2.5 turbulence closure model that was originally formulated by Furuichi et al. (2012). The governing equations for temperature (T), salinity (S), and horizontal velocity (u and v represent zonal and meridional velocity, respectively) in the 1-D ML model are as follows:

$$\frac{\partial T}{\partial t} = \frac{\partial}{\partial z}(\kappa_T \frac{\partial T}{\partial z}) + \frac{1}{\rho_0 C_p}\frac{\partial I}{\partial z} + Res_T(t,z) \tag{1}$$

$$\frac{\partial S}{\partial t} = \frac{\partial}{\partial z}(\kappa_S \frac{\partial S}{\partial z}) + Res_S(t,z) \tag{2}$$

$$\frac{\partial u}{\partial t} = f(v - v_{geo}) + \frac{\partial}{\partial z}\left(\kappa_V \frac{\partial u}{\partial z}\right) + Res_u(t,z) \tag{3}$$

$$\frac{\partial v}{\partial t} = -f(u - u_{geo}) + \frac{\partial}{\partial z}(\kappa_V \frac{\partial v}{\partial z}) + Res_v(t,z) \tag{4}$$

where ρ_0 (=1023 kg m^{-3}) is the reference density, C_p (=3940 J kg^{-1} K^{-1}) the specific heat of the seawater, I the penetrating shortwave radiation, and f the Coriolis parameter. Here, the shortwave penetration was computed by assuming the Jerlov water type IA (Paulson & Simpson, 1977). κ_T, κ_S, and κ_V denote the vertical diffusion coefficients of heat, salt, and momentum, respectively, and are internally computed in the model by the turbulence closure scheme, which is primarily based on the local density stratification (calculated from T and S) and vertical shear of horizontal currents at each vertical level (see Furuichi et al. (2012) for details). The major update from Kido & Tozuka (2017) is the implementation of geostrophic velocity (u_{geo}, v_{geo}), which is externally added to the model as the boundary condition. This modification is essential for the better simulation of velocity fields in the midlatitude ocean, particularly over regions with swift currents. The last term in each equation, namely $Res_T(t,z)$, $Res_S(t,z)$, $Res_u(t,z)$, and

$Res_v(t, z)$, are referred to as the dynamical correction term, and it represents a contribution from the three-dimensional processes (e.g., horizontal and vertical advection), which cannot be explicitly treated in the 1-D framework. These terms are estimated on the basis of the specified temperature, salinity, and horizontal velocity as described below using technique proposed in Kido & Tozuka (2017). To summarize, the external forcing components necessary for conducting the model experiment are surface atmospheric forcing (heat, freshwater, and momentum fluxes), geostrophic current fields, and three-dimensional oceanic variables used for the initializations and computations of the dynamical corrections. Such implicit incorporations of advective effects into the 1-D ML model have also been adopted in other studies (Vivier et al., 2002), and shown to realistically serve as a substitute for the 3-D dynamical processes. For more comprehensive descriptions of our 1-D ML model, interested readers are referred to Furuichi et al. (2012) and Kido & Tozuka (2017).

In this study, the 1-D ML is configured at each grid point over a domain covering the western North Pacific region (135°–170°E, 30°N–50°N) with 0.5° longitude × 0.5° latitude. The model has a variable vertical resolution, from 2 m near the surface to 10 m at the bottom (the maximum depth is set to 1000 m). Daily shortwave/longwave radiation, 10 m winds, air temperature, specific humidity, and monthly precipitation from J-OFURO3 (Tomita et al., 2019) are used to force the model. Turbulent heat flux, evaporation, and wind stress are calculated using the bulk formulae of Kara et al. (2005). Geostrophic currents are calculated using the density field of the FORA-WNP30, assuming a level of no motion at 2000 m. Initial and restoring conditions (three-dimensional profiles of temperature, salinity, and horizontal current) are then taken from the FORA-WNP30.

Using atmospheric and oceanic forcing as outlined above, we first conducted a preliminary experiment to obtain the dynamical correction terms necessary for the realistic simulation of oceanic variability in the KOCR. For this experiment, the model was initialized from October 15 of each year from 1991 to 2012 and then integrated forward for 12 months with atmospheric forcing and geostrophic currents, while restoring the modeled temperature, salinity, and horizontal velocity toward the values derived from the FORA-WNP30 with a nudging time scale of 5 days. During the integration of this experiment, the dynamical correction terms (e.g., $\frac{T_{FORA}-T}{5\,[days]}$ in the case of temperature, where T_{FORA} denotes the temperature value of the FORA-WNP30) were computed at each time step and stored as 1-day averaged values for use in the subsequent experiments. These dynamical corrections were essential for realistically constraining the time evolution of the temperature and horizontal velocity in the subsequent sensitivity experiments. Next, we performed the control (CTL) experiments, for which the model was initialized and integrated with the same atmospheric and oceanic conditions with those in the preliminary experiment, but the nudging of the temperature and horizontal velocity was turned off and the dynamical correction terms obtained from the preliminary integrations were used instead (note that salinity was still relaxed to the FORA-WNP30's value with the nudging time scale of 5 days). As in the preliminary experiment, the CTL experiment was also conducted for all years from 1991 to 2013 in order to simulate the observed variations in the KOCR. As the dynamical correction terms were archived with a high temporal resolution (1-day averaged values were used), the temperature, salinity, and current fields from the CTL experiment were very similar to, or nearly identical, to those from the preliminary experiment (figures not shown). This experiment was used as a reference for comparison to the sensitivity experiment described in Section 4.2.

3. Features of salinity variation in the KOCR

3.1 Features

First, we examine the time series of temperature and salinity anomalies averaged over the KOCR (142°–153°E, 36°–40°N; see the inset black box in Fig. 1g) obtained from the Argo product and FORA-WNP30 (Figs. 2a, b). Note that this box is chosen to adequately cover the transition region between the Kuroshio Extension (KE) and the Subarctic Front (Kida et al., 2015). Over the KOCR, SST and SSS anomalies exhibit coherent interannual to decadal fluctuations, and their time evolution in the Argo product agree well with those in the FORA-WNP30. Indeed, the temporal correlation coefficient between the Argo product and FORA-WNP30 was 0.67 for SST and 0.62 for SSS, both of which were statistically significant at a 90% confidence level based on the bootstrap method (here, we have generated 10,000 randomly ordered data and estimated the confidence intervals of the correlation coefficients). The spatial patterns of climatological surface and subsurface temperature and salinity over the KOCR also agreed well between the Argo and FORA-WNP30 (figures not shown). For these reasons, we conclude that the FORA-WNP30 adequately reproduced the observed oceanic variability in this region. More thorough validations of the FORA-WNP30 against various observational data are presented by Usui et al. (2017).

To delineate the seasonality of salinity variation, the standard deviation of interannual variability of area-averaged SSS anomalies over the KOCR and their correlation coefficient with SST anomalies over the same region were calculated for each calendar month (Figs. 2c, d). In both the Argo and reanalysis products, the peak of the SSS variation was found to be around the boreal spring, although the FORA-WNP30 slightly underestimated the observed amplitude (Fig. 2c). The coherence between the temperature and salinity was also strong during this season (Fig.

2d), while it was relatively weak during the summer and fall. Considering this seasonality of SSS variability and annual cycle of MLD, in the analysis that follows, we will primarily focus on the salinity variation during the late winter to boreal spring (February-April averaged values).

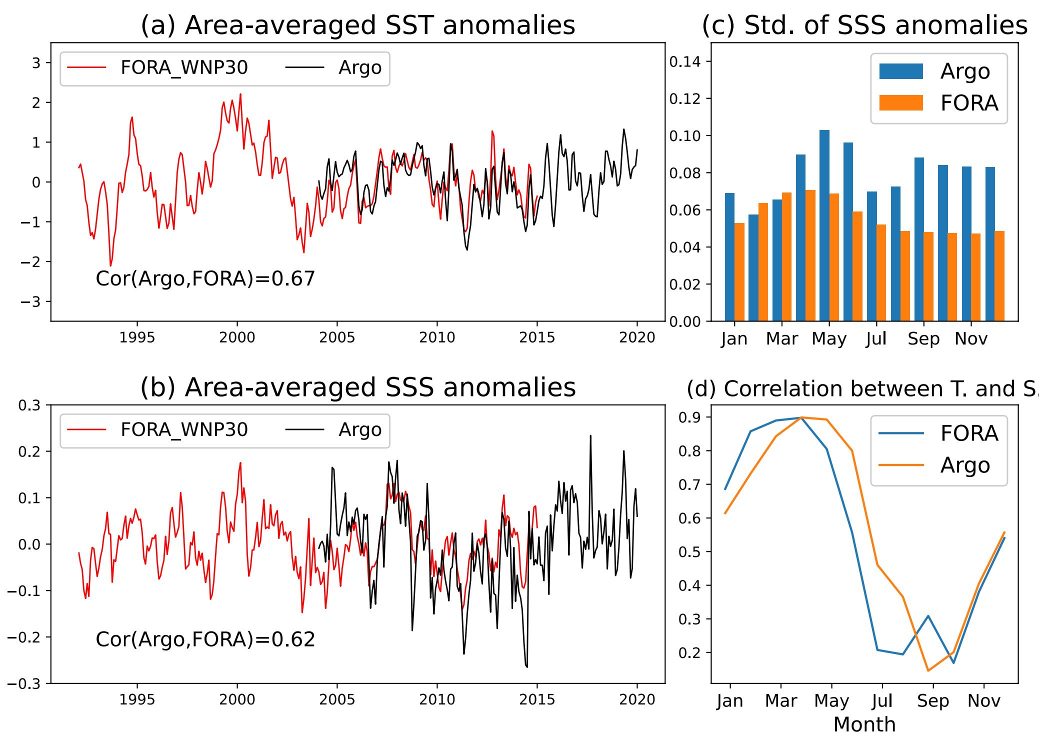

Figure 2. (a) Time series of 3-month averaged SST and (b) SSS anomalies averaged over the KOCR (142°E–153°E, 36°N–40°N; see black box in Fig. 1g) from the Argo product (black) and FORA-WNP30 (red). Note that anomalies of the Argo product (FORA-WNP30) are relative to their seasonal mean values from 2004 to 2019 (1991 to 2013). The correlation coefficients between the Argo product and FORA-WNP30 are shown in the lower left. (c) Standard deviation of the SSS anomalies averaged over the KOCR as a function of calendar months from the Argo product (orange) and FORA-WNP30 (blue). (d) As in (c), but for correlation coefficients

between SST and SSS anomalies over the KOCR. The unit for SST (SSS) is °C (psu).

As can be seen in the time series of SST and SSS anomalies (Figs. 2a, b) and their correlation (Fig. 2d), anomalous saltening (freshening) in the KOCR tends to co-occur with warming (cooling) therein. To objectively detect such anomalous events and extract features common to all cases, we will define positive and negative years as follows: a positive (negative) year is defined as one with both February to April averaged SST and SSS anomalies over the KOCR that are larger (smaller) than their 0.5 standard deviation. According to this criterion, 6 (8) positive years and 4 (6) negative years can be identified in the Argo data (FORA-WNP30) (Table 1).

	Positive years	Negative years
Argo (RG09)	2007, 2008, 2009, 2013, 2016, 2019 (6 events)	2011, 2012, 2014, 2015 (4 events)
Reanalysis (FORA-WNP30)	1997,1999, 2000, 2002, 2007, 2008, 2009, 2013 (8 events)	1996, 2003, 2004, 2005, 2010, 2011 (6 events)

Table 1. Positive and negative years identified in the Argo data (RG09) and reanalysis product (FORA-WNP30).

Composites of the temperature and salinity field during the mature phase of positive and negative years (averaged for February-April) obtained from the Argo product are shown in Fig. 3. We note here that the features in the composites with January–March mean are qualitatively similar to the following composites. During positive years, warm and saline water from the subtropical region extends farther to the north compared to negative ones (Figs. 3a, b, d, e). As expected from the definition of events, regions with significant differences in SST tend to be collocated with those in SSS (Figs. 3c, f). Similar patterns are also found in composites from the FORA-WNP30 (Fig. 4), although small-scale features are more evident and the amplitude of SSS anomalies is slightly smaller than that in the Argo data. As the gross features of composite fields constructed from the Argo data of the overlapping period (2004-2013) were very similar to the original ones (figures not shown), quantitative differences between the Argo and FORA-WNP30 may be caused by those in their horizontal resolution and analysis method, rather than the analysis period. Such anomalous warming events in the KOCR have also been noted in several previous studies (Masunaga et al., 2016; Qiu et al., 2017; Sugimoto et al., 2014); however, these studies have not specifically focused on associated salinity variations. These studies have pointed out that the low-frequency fluctuations of SST over the KOCR are related to the modulation of dynamic states of the KE. To determine whether such arguments also apply to our selected positive/negative years, we will explore the origin of these temperature and salinity variations in the next subsection.

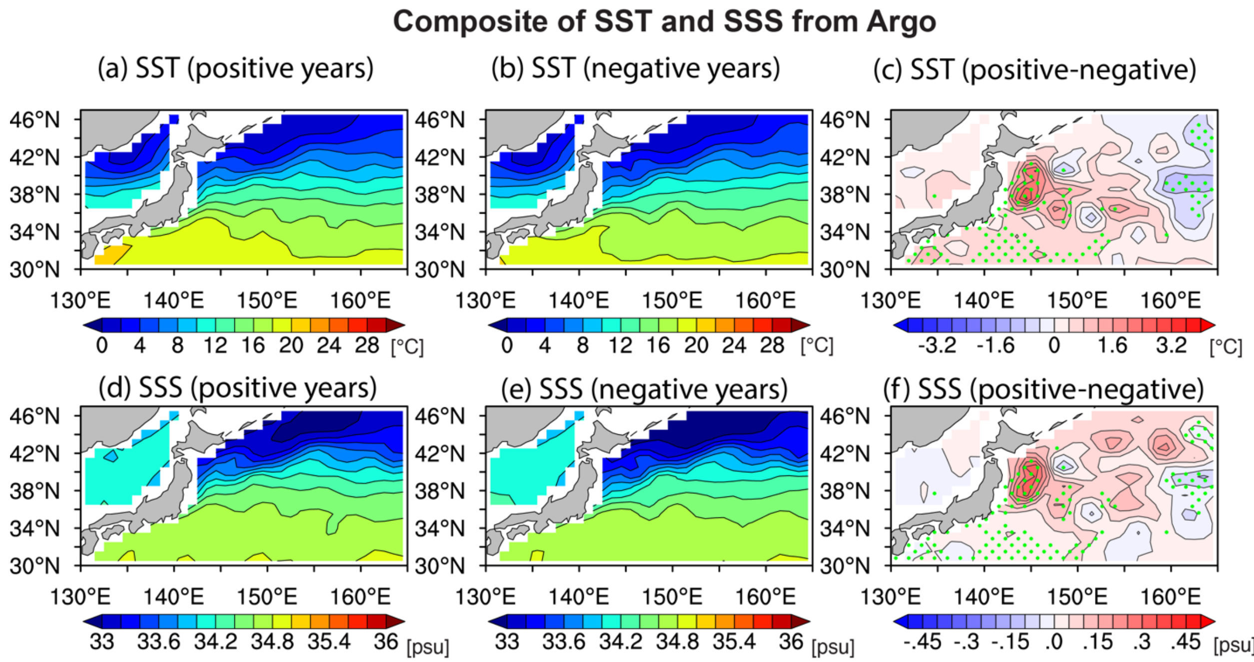

Figure 3. (a)–(c): Composite of SST fields (in °C) during February-April of (a) positive and (b) negative years from the Argo data. Differences between positive and negative years (i.e. (a) minus (b)) are shown in (c). The contour intervals in (a) and (b) are 2, whereas those in (c) are 0.4. Differences that are significant at the 80% confidence levels based on a two-tailed t-test are green dotted in (c). (d)–(f): As in (a)(c), but for SSS fields (in psu). The contour intervals in (d) and (e) are 0.2, whereas those in (f) are 0.05.

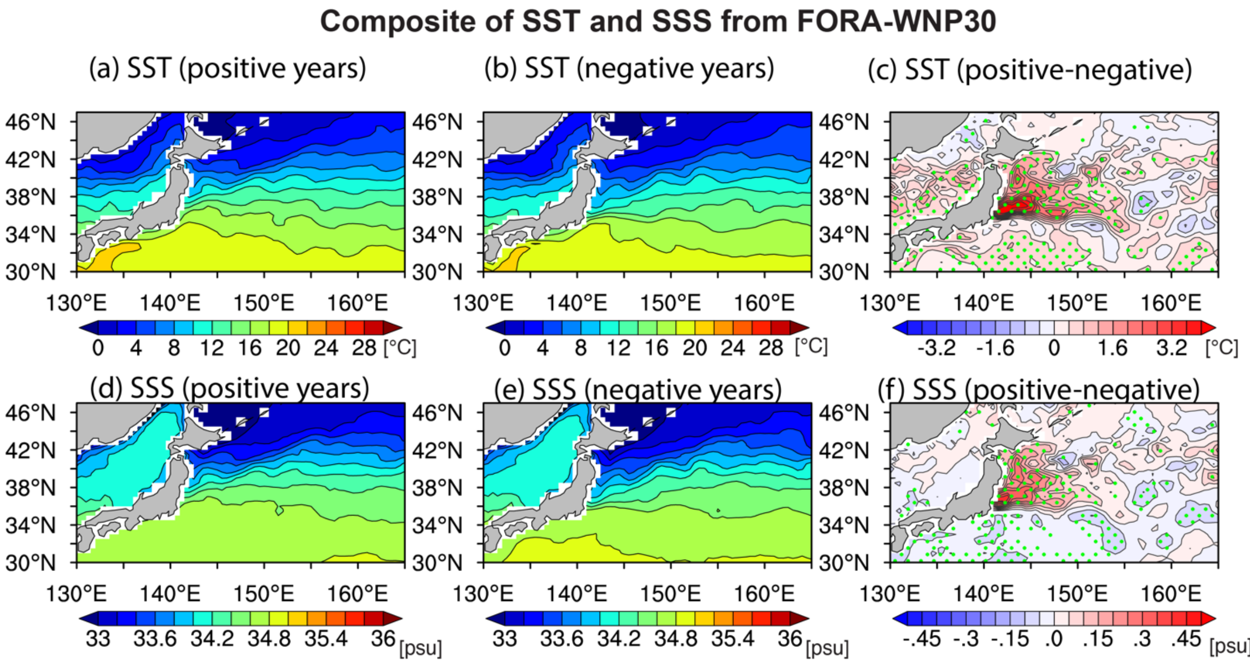

Figure 4. As in Fig. 3, but from the FORA-WNP30.

To examine the driving mechanisms of temperature and salinity variations over the KOCR, it is helpful to emphasize their vertical structure. For this purpose, latitude-depth sections of zonally averaged (142°–153°E) composited temperature, salinity, and potential density from the Argo data are depicted in Fig. 5. For both positive and negative years, prominent density-compensating temperature and salinity fronts are seen around 36°-39°N and they extend to the upper 200 m (Figs. 5a, b, d, e). Comparison of the temperature and salinity fields between the positive and negative years reveals that strong warming and saltening is observed in the KOCR during the positive years, while the opposite is observed in the negative years (Figs. 5c, f). Large differences in temperature and salinity are found near the surface to the north of 38°N (i.e., the subarctic region), whereas they are found near the thermocline depth (from 200 to 400 m depth) to the south (Figs. 5c, f). Such latitudinal differences in the vertical structures of low-frequency thermohaline anomalies have also been noted by Nonaka et al. (2006).

Interestingly, the differences in potential density are characterized by meridional dipole structures (Fig. 5i) with negative anomalies (i.e., a decrease in density) to the south and positive anomalies to the north. The causes of these density anomalies will be discussed in the next section by decomposing these anomalies into respective contributions from temperature and salinity. Similar patterns of temperature, salinity, and potential density anomalies are also observed in composited fields obtained from the FORA-WNP30, although anomalies over the northern part are slightly underestimated (Fig. 6). Hence, we believe that the differences in the upper ocean fields between the positive and negative years are robust features across the datasets and analysis periods. In the next subsection, we will explore the governing mechanisms of these events and possible links to large-scale variability by inspecting the features of other variables.

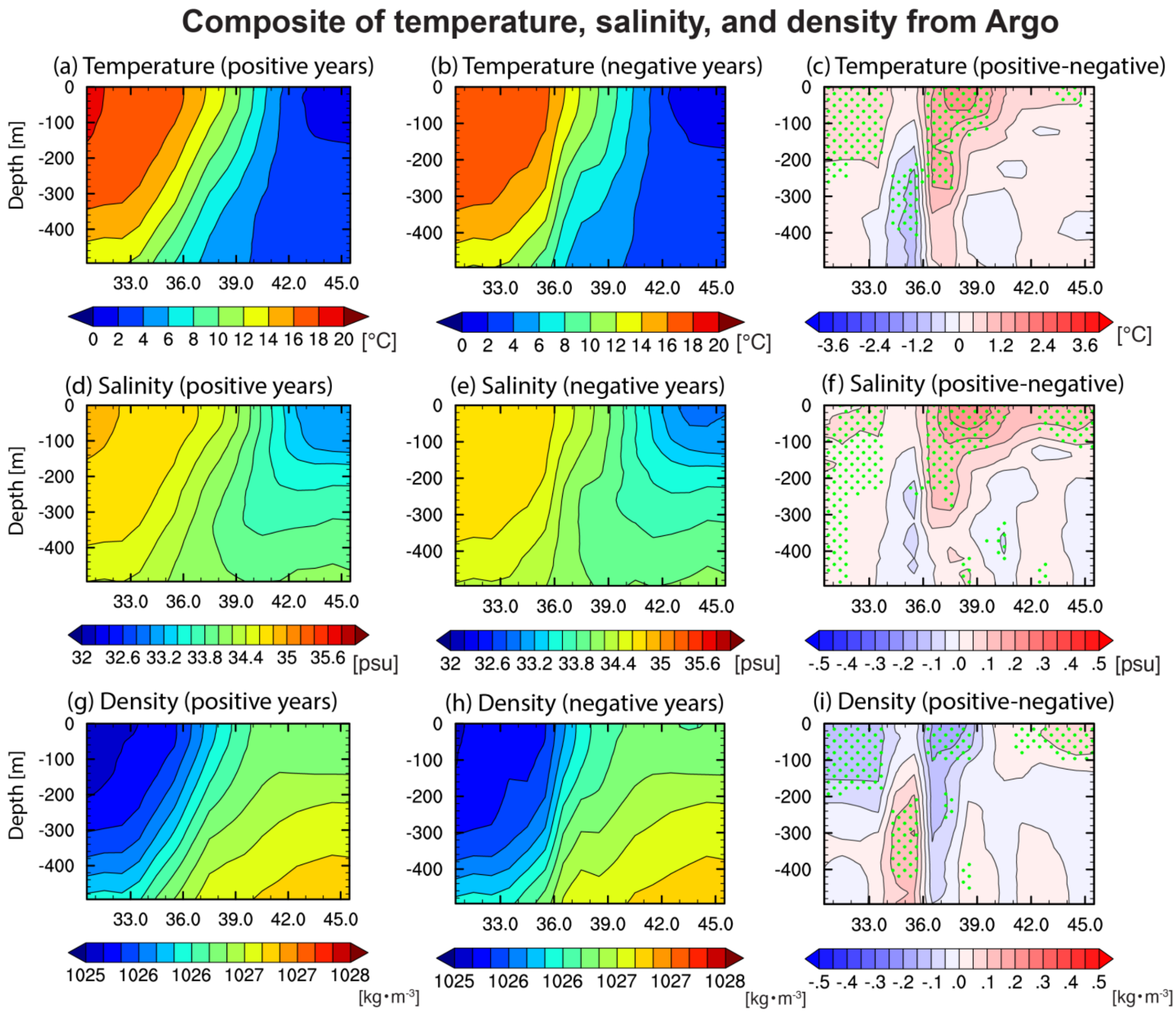

Figure 5. (a)–(c): Latitude-depth section (zonally averaged from 142°-153°E) of composited temperature (in °C) fields during February-April of (a) positive and (b) negative years, and (c) their differences from the Argo data. The contour intervals are 2 in (a) and (b), whereas those in (c) are 0.4. Differences that are significant at the 80% confidence levels based on a two-tailed t-test are green dotted in (c). (d)–(f): As in (a)–(c), but for salinity fields (in psu). The contour intervals are 0.2 in (d) and (e), and those in (f) are 0.05. **(g)–(i)**: As in (a)–(c), but for potential density

fields (in kg m^{-3}). The contour intervals are 0.2 in (g) and (h), whereas those in (i) are 0.05.

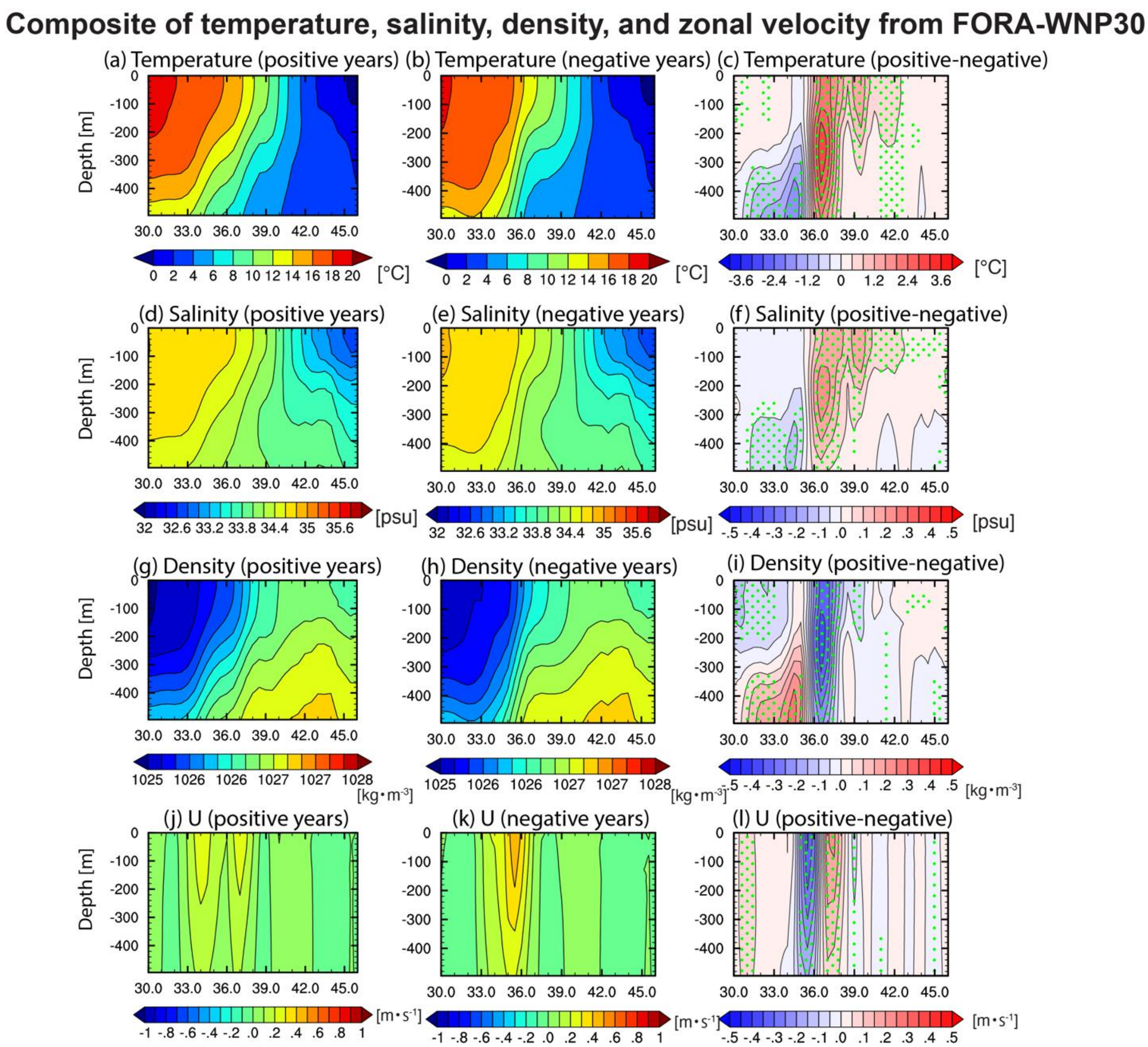

Figure 6. (a)–(i): As in Fig. 5, but from the FORA-WNP30. (j)–(l): As in (a)–(c), but for the zonal current fields (in m s^{-1}). The contour intervals in (j) and (k) are 0.1 and 0.05 in (l).

3.2 Mechanisms

There are several candidates that induce co-variations in temperature and salinity variations over the KOCR. First, changes in the local atmospheric conditions, such as anomalous heat and freshwater exchanges at the sea surface can directly generate in-phase and/or out-of-phase variations in SST and SSS. Second, an anomalous strengthening or weakening of large-scale ocean circulation (both the Ekman and geostrophic current) may modulate temperature and salinity advection, thereby creating significant anomalies. Third, a modulation in the strength of the mesoscale eddy activities affects the magnitude of the eddy-induced transport of heat and freshwater transport, thereby leading to significant temperature and salinity anomalies. To identify relative contribution from these factors and underlying physical processes, composites of various physical parameters are presented in Figure 7. Because the growing season of temperature and salinity anomalies in the KOCR is a few months prior to the mature phase (the lead–lag relationship between the SSS anomalies and SSS tendency anomalies is shown in Fig. 8), we focus on differences averaged from December to February.

Due to the outbreak of cold and dry air masses from the continent by the westerly wind, the net surface heat flux is mostly upward (i.e., the ocean releases heat into the atmosphere) over the western North Pacific (Figs. 7a, b). Differences between the positive and negative years (Fig. 7c) show that the ocean is more strongly cooled by the atmosphere during the positive years in the KOCR. A detailed decomposition of the heat flux anomalies into individual components (i.e., shortwave and longwave radiation as well as sensible and latent heat fluxes) reveals that warmer SST during the positive years (Fig. 3c) and associated increases in the turbulent heat fluxes are responsible for the total differences (figures not shown). Therefore, the heat flux anomalies serve to dampen the SST anomalies and do not contribute to their generation and growth. These results are in line with those from previous observational studies, which underlined the importance of SST anomalies over the Kuroshio and Oyashio extension regions in driving heat flux variability there (Masunaga et al., 2016; Sugimoto & Hanawa, 2011; Tanimoto et al., 2003).

Consistent with the heat flux fields and their interpretation described above, more (less) freshwater is lost to the atmosphere over the KOCR during the positive (negative) years (Figs. 7d–f). This is conducive to surface saltening (freshening) in the positive (negative) years and could contribute to the generation of the observed SSS anomalies. Unsurprisingly, these differences in freshwater fluxes are primarily due to changes in evaporation, while no significant differences were found in the precipitation fields. The maximum amplitude of freshwater flux differences is approximately 2×10^{-8} m s^{-1}, which leads to changes in the mixed layer salinity of 0.02 psu per month, assuming the mixed layer depth of 100 m. This value is rather smaller than the observed total SSS differences (~0.2 psu) and could explain only one–third of the anomaly in three months, suggesting that other processes, such as anomalous salinity advection, may also be important for the generation of salinity variations.

To highlight the roles played by oceanic processes, we next compare low-passed sea surface height, surface current, and eddy kinetic energy (EKE) fields between positive and negative years (Figs. 7g–l). Here, the low-frequency (high-frequency) signals were obtained by applying a 300-day (Qiu & Chen, 2005) Lanczos low-pass (high-pass) filter (Duchon, 1979) to the total fields.

Differences in the SSH fields between the positive and negative years are characterized by a meridional dipole over the KE, with the higher (lower) SSH anomalies to the north (south) of the climatological eastward jet (Fig. 7i). More specifically, the signatures of the southern and northern recirculation gyres (Qiu et al., 2008) are markedly discernable and the KE jet is zonally oriented during negative years (Fig. 7h), whereas the KE jet is weaker and convoluted during positive ones (Fig. 7g). These features are suggestive of their link with the bimodal states of the KE (Qiu & Chen, 2005, 2010; Taguchi et al., 2010); a positive (negative) year with weaker recirculation gyres corresponding to an unstable (stable) state of the KE, as speculated in several previous studies (Masunaga et al., 2016; Qiu et al., 2017; Sugimoto et al., 2014). The differences in velocity fields (figures not shown) are nearly in geostrophic balance with those in SSH, suggesting that current anomalies mostly come from the geostrophic components rather than the Ekman current. During positive years, northeastward currents over the KOCR are more prominent than negative years, especially in the southwestern area (36°N–38°N; see also Figs. 6g–l). The stronger (weaker) northeastward current during positive (negative) years leads to an increase (a decrease) in the advection of warm and salty water from the south, contributing to an anomalous warming and saltening (cooling and freshening) over the KOCR. Such a modulation of advective processes efficiently operates in the climatological frontal regions with strong temperature and salinity gradients and may partly explain the differences in the peak depth of anomalies between the northern and southern areas of the KOCR (Nonaka et al., 2006). The region with significant current anomalies collocates with upstream portions of the quasi-stationary jet (QSJ, also referred to as the J-1) (Isoguchi et al., 2006; Wagawa et al., 2014), which is a conveyor of warm and saline water from the KE to subarctic regions. Thus, these current anomalies may be viewed as a modulation of the QSJ associated with changes in the dynamical state of the KE, as suggested in an observational study by Wagawa et al. (2014).

In relation to changes in large-scale ocean circulation, the strength of mesoscale eddy activity undergoes significant variations due to changes in barotropic/baroclinic instability as well as those in the interaction with bottom topography (Qiu & Chen, 2005, 2010; Yang et al., 2017). With respect to the KE, the EKE in the upstream regions substantially decreases when it is in a stable state; conversely, the EKE increases when the KE is in an unstable state. (Itoh & Yasuda, 2010; Qiu & Chen, 2005, 2010; Sasaki & Minobe, 2015; Sugimoto et al., 2014; Taguchi et al., 2010). To confirm consistency with these previous findings, we calculated the EKE as follows:

$$EKE = \frac{1}{2}\left(u'^2 + v'^2\right), \quad 5)$$

where (u', v') denotes high-passed horizontal velocity.

During positive years, an elevated EKE level is seen during positive years compared to negative years (Figs. 7j–l), supporting our argument that the positive (negative) years correspond to an unstable (stable) and high eddy-activity state of the KE. As individual mesoscale eddies serve to relax the meridional gradients of temperature and salinity through Lagrangian transports of heat and salt (Dong et al., 2017; Itoh & Yasuda, 2010), the increase (decrease) in numbers and strength of mesoscale eddies during the positive (negative) years is conducive for warming and saltening (cooling and freshening) over the KOCR (Qiu et al., 2017; Sasaki & Minobe, 2015; Sugimoto et al., 2014), as well as anomalous large-scale ocean circulation.

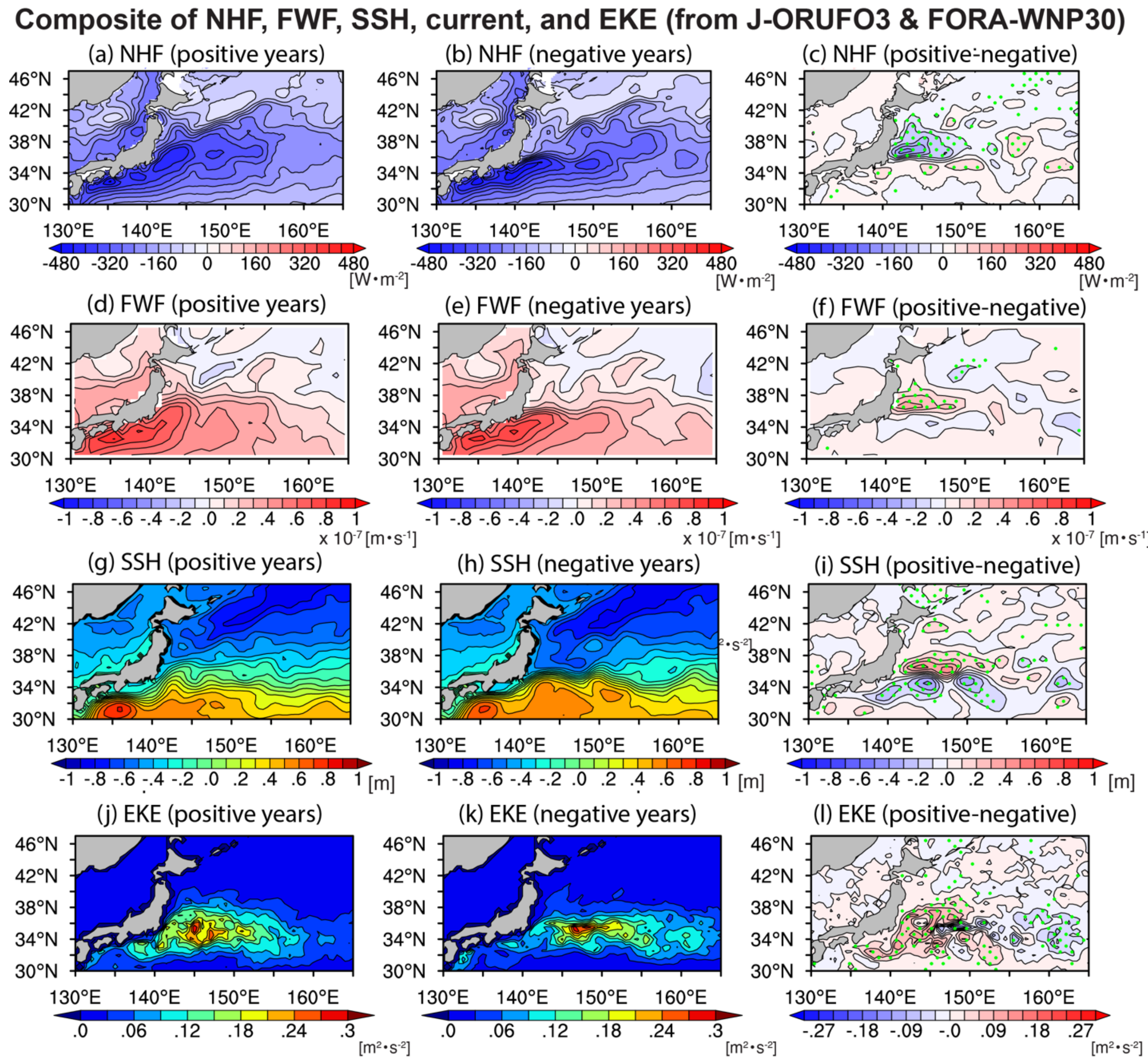

Figure 7: (a)–(c): Composite of net surface heat flux (in W m^{-2}) during December-February of (a) positive and (b) negative years, and (c) their differences from the J-OFURO3. The contour intervals are 50. Here, positive values indicate heating of the ocean by the atmosphere. Differences that are significant at the 80% confidence levels based on a two-tailed t-test are green dotted in (c). (d)–(f): As in (a)–(c), but for net surface freshwater flux (evaporation minus precipitation) (in m

s^{-1}). The contour intervals are 1×10^{-8}. (g)–(h): As in (a)–(c), but low-passed sea surface height (in m). The contour intervals are 0.1. (j)–(l): As in (a)–(c), but for the surface eddy kinetic energy (EKE: in $m^2 s^{-2}$). The contour intervals are 0.03.

To confirm the importance of the various processes described above, lead–lag correlation coefficients between February-April mean SSS anomalies over the KOCR and other variables are presented in Fig. 8. As mentioned in Section 3.1 (Fig. 2d), SSS anomalies are highly correlated with SST anomalies over the same region, with its maximum value around lag 0 (Fig. 8, black curve). The SSS tendency (i.e., the time derivative of SSS) has a significant positive correlation with SSS anomalies when the former lead the latter by around 2 to 6 months, suggesting that the maximum growth of SSS anomalies occurs a few months before their peak season (grey curve). The freshwater flux anomalies (note that they are defined as evaporation minus precipitation, so that the positive values correspond to increases in SSS) also exhibit significant correlations, but their coefficients are relatively low (~0.4), when they lead the SSS anomalies (blue curve). Similar features with a reversed sign were also found for the net heat flux anomalies (figure not shown). Therefore, the local atmospheric anomalies are not the main driver of the observed temperature and salinity variations, although they may play a secondary role in determining their amplitude.

For ocean dynamical variables, both zonal and meridional low-pass filtered velocity (orange and green curves) and EKE anomalies are significantly correlated with SSS with leading SSS anomalies, supporting the idea that the temperature and salinity variations over the KOCR are closely linked to the dynamical state of the KE. As the ocean background circulations and mesoscale eddy fields mutually affect each other via eddy-mean flow interaction (Qiu & Chen, 2010; Taguchi et al., 2010), it is not straightforward to clearly isolate individual contributions from both factors. Therefore, herein we qualitatively conclude that changes in the stability of the KE path leads to coherent changes in the upper ocean temperature and salinity over the KOCR through modulation of heat and salt transport by large-scale geostrophic current and mesoscale eddies, whereas contributions from freshwater flux and Ekman advection anomalies seemed to be not so important. A comparison of advective terms estimated from the current fields and salinity of the FORA-WNP30 also corroborated the above conclusion (Fig. S1). For a more quantitative and comprehensive assessments of these processes, a closed salinity budget analysis based on a realistic high-resolution ocean model is desirable and could be an interesting topic for future studies.

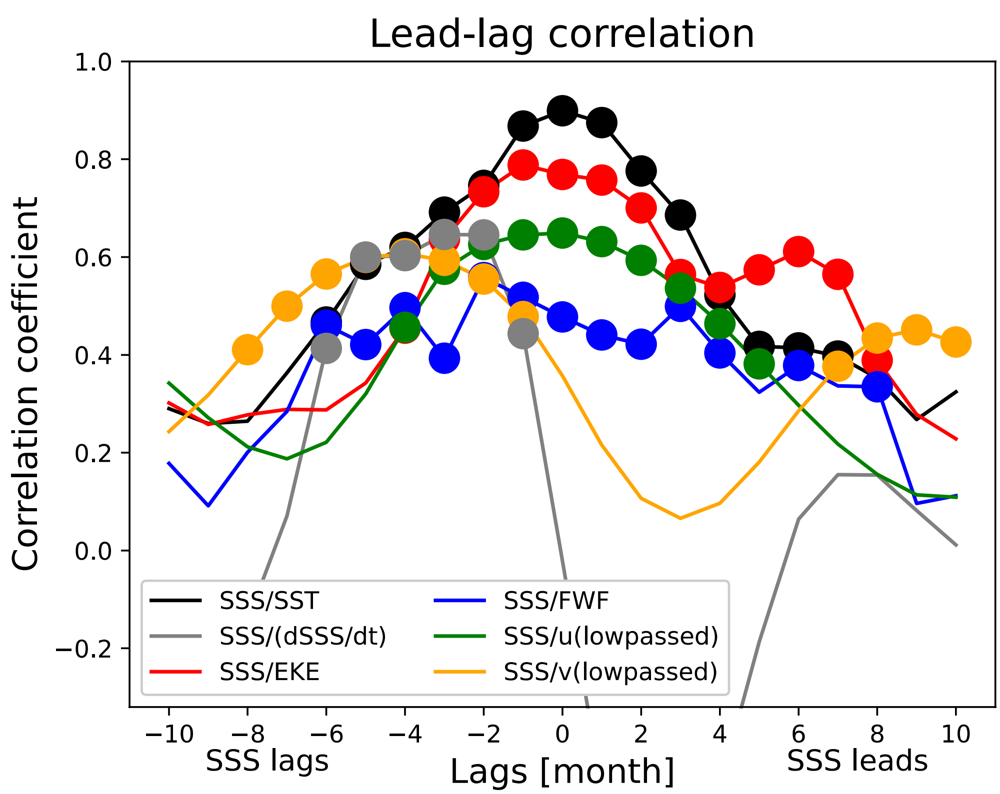

Figure 8. Lead–lag correlation coefficients between February-April averaged SSS anomalies over the KOCR and other variables (black: SST; grey: SSS tendency; red: EKE; blue: freshwater flux; green: low-passed surface zonal velocity; and orange: low-passed surface meridional velocity). All oceanic variables (SSS, SST, EKE, surface velocity) are taken from the FORA-WNP30 reanalysis, whereas the J-OFURO3 product is adopted for the freshwater flux. The lag is in units of the month, and positive (negative) values indicate SSS anomaly leads (lags). Correlation coefficients that are significant at the 90% confidence levels on the basis of the bootstrap method are represented by the colored dots.

4. Impact of salinity variation

In this section, we assess how these salinity variations can alter the upper ocean's hydrographic properties and eventually affect the evolution of the SST, which is a key variable for midlatitude air–sea interaction.

4.1 Temperature and salinity contributions to density anomalies

We calculate the potential density of seawater (denoted as $\rho(T,S)$) using original (i.e. interannually varying) temperature and salinity based on the equation of state by Jackett &Mcdougall (1995). Then, we compute the potential density using original temperature and climatological salinity (represented by $\bar{S}$), $\rho_T = \rho(T,\bar{S})$, to isolate the effect of salinity variations. Differences in potential density between the positive and negative years, $\Delta\rho = \rho_{POS}(T,S) - \rho_{NEG}(T,S)$, contain both contributions from temperature and salinity differences. For ρ_T, $\Delta\rho_T = \rho_{POS}(T,\bar{S}) - \rho_{NEG}(T,\bar{S})$) are caused only by the temperature difference. Thus, the contribution from salinity variations to potential density ($= \Delta\rho_S$) can be estimated by considering the differences between $\Delta\rho$ and $\Delta\rho_T$, i.e. $\Delta\rho_S = \Delta\rho - \Delta\rho_T = \{\rho_{POS}(T,S) - \rho_{POS}(T,\bar{S})\} - \{\rho_{NEG}(T,S) - \rho_{NEG}(T,\bar{S})\}$). Although the nonlinearity of the equation of state does not allow a complete separation of the density signals into temperature and salinity contributions, this method is useful for illustrating the importance of salinity variations. Differences in other density-dependent variables, such as the buoyancy frequency and mixed layer (see below for detailed definitions) can, in the same manner, be decomposed into temperature and salinity contributions. This approach has been widely used for assessments of salinity impacts over the tropical Pacific (Zheng & Zhang, 2012, 2015) and tropical Indian Ocean (Kido & Tozuka, 2017).

The positive temperature and salinity anomalies in the KOCR in the positive years (Figs. 9a, b; see also Figs. 3c, f) serve compensate each other in forming anomalous densities, with positive temperature anomalies leading to a decrease in sea surface density (SSD) (Fig. 9c), whereas positive salinity anomalies contribute to increases in the SSD there (Fig. 9d). As a result, negative values of the total SSD differences are confined to the southern part of the KOCR (south of 38°N; Fig. 9e). Similar features are also evident in composites from the FORA-WNP30, although surface saltening and associated compensations of the temperature-related SSD signals are weaker than those in the Argo data (Figs. 10a–e).

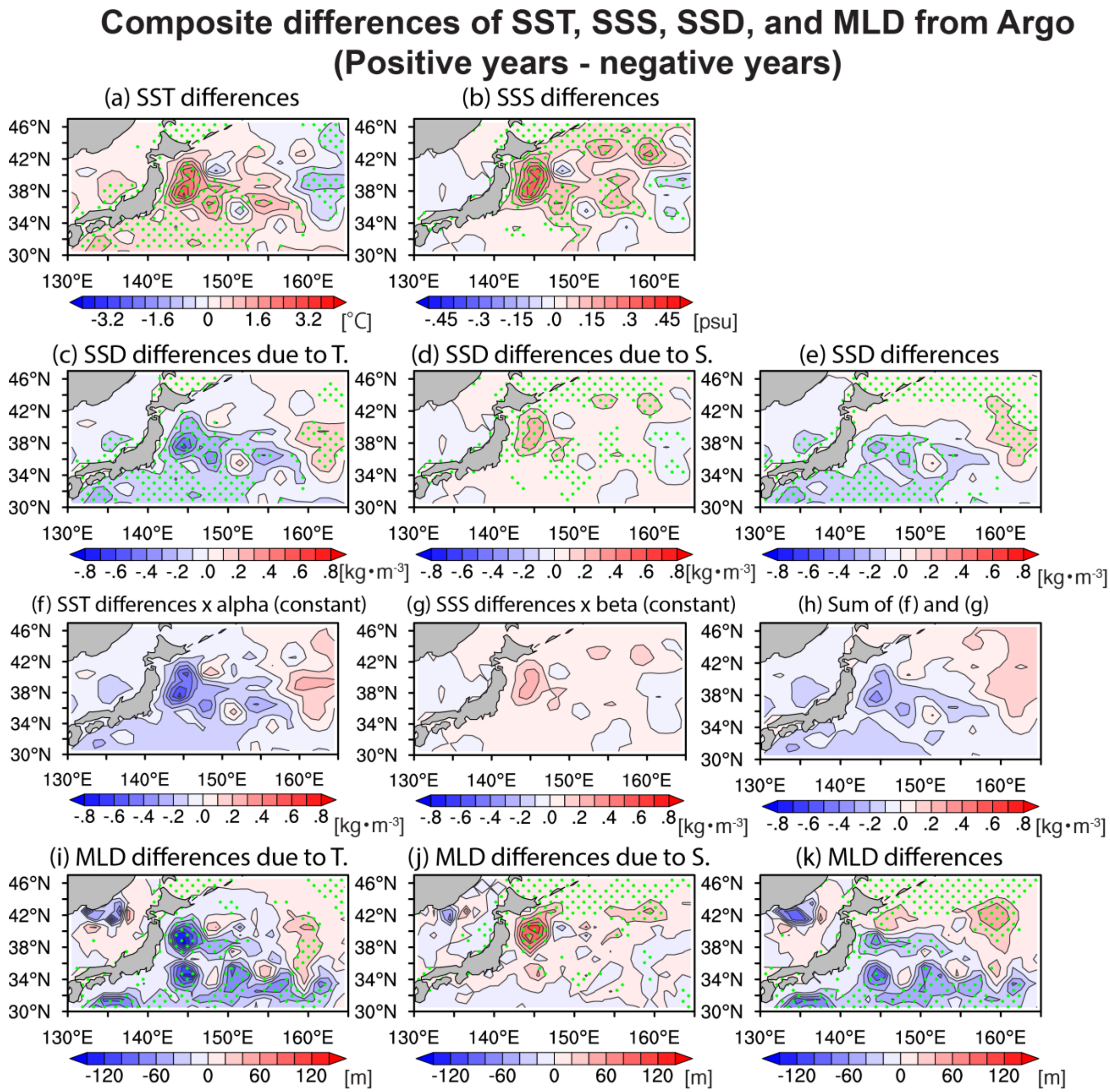

Figure 9. (a), (b): Differences in composited (a) SST (in °C) and (b) SSS (in psu) fields between positive and negative year during February-April. The contour intervals in (a) are 0.4, whereas those in (b) are 0.05. (c)–(e) As in (a) and (b), but for (e) shows the surface density differences and contribution from (c) SST and (d) SSS differences (in kg m^{-3}). The contour intervals are 0.08 (see the main text

for details of the decomposition method). (f): Sea surface density differences estimated from SST differences, assuming a uniform thermal expansion coefficient (i.e. (a) multiplied by –0.22 kg °C^{-1} m^{-3}) (in kg m^{-3}). The contour intervals are 0.08. (g), as in (f), but from SSS differences assuming uniform saline contraction coefficients (i.e., (b) multiplied by 0.77 kg psu^{-1} m^{-3}). The sum of (f) and (g) is shown in (h). (i)–(k): As in (c)–(e), but for the mixed layer depth differences (in m). The contour intervals are 20. Differences that are significant at the 80% confidence levels on the basis of a two-tailed t-test are green dotted (except for (f)-(h)). All panels are from the Argo data.

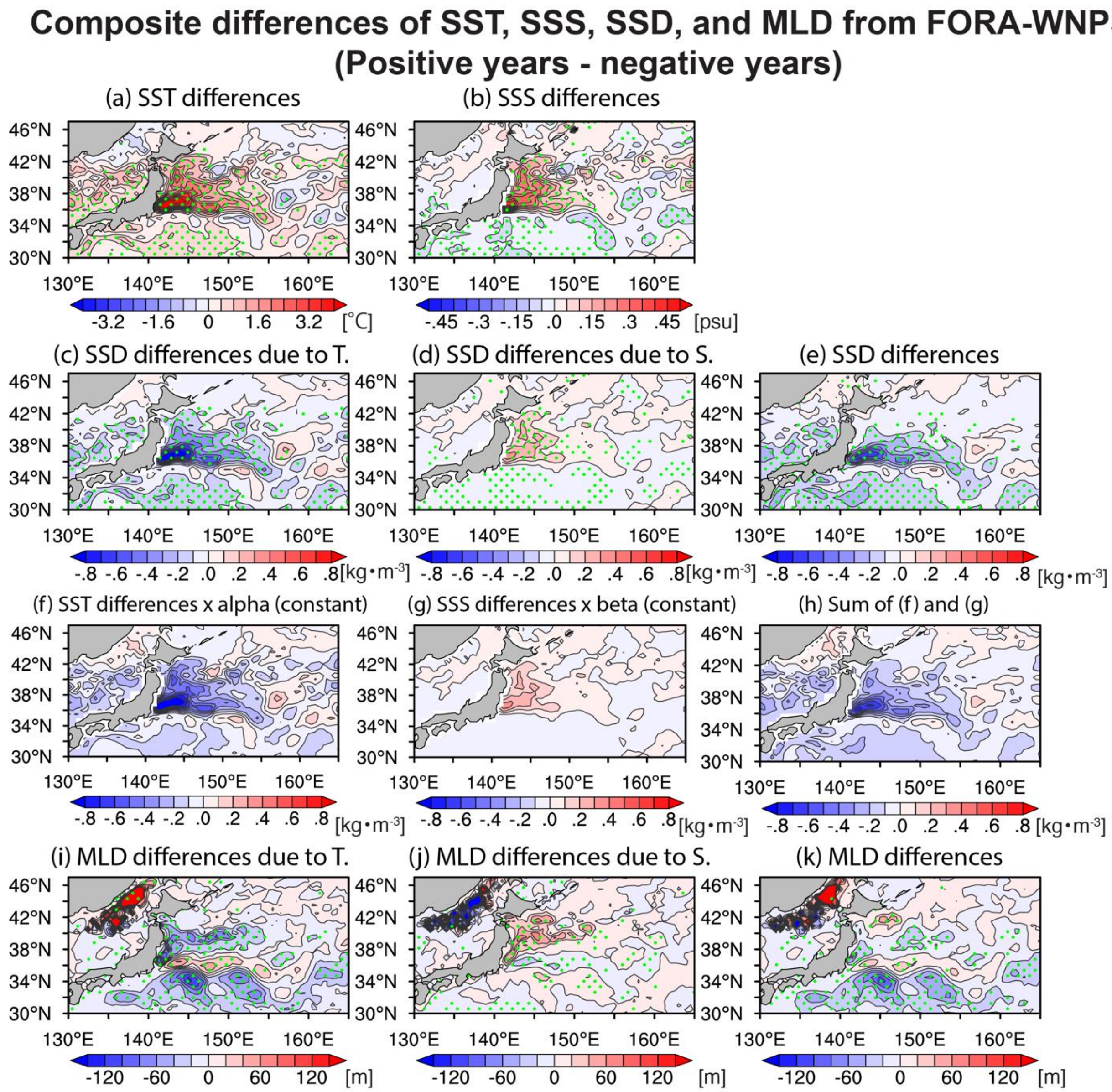

Figure 10. As in Fig. 9, but from the FORA-WNP30.

A noticeable feature in the composite field is the fact the spatial pattern of SST's contribution to SSD (Figs. 9c) is somewhat different from that of the original SST differences (Figs. 9a), and such discrepancies are not found in the SSS fields (Figs. 9b, d) (see also Fig. 10 for the FORA-WNP30). Specifically, SST's contribution to SSD is relatively weak in higher latitudes compared to the distribution of the original SST differences. This could be due to lower background SST and weaker dependence of density on temperature at higher latitudes. To confirm this argument, we converted SST and SSS anomalies into SSD using a linear relation. Assuming the linearity of the equation of state, the differences of potential density can be approximated as follows:

$$\Delta\rho = \Delta\rho_T + \Delta\rho_S \simeq \alpha(T_{POS} - T_{NEG}) + \beta(S_{POS} - S_{NEG}) = -\alpha\Delta T + \beta\Delta S,$$

where α and β represent thermal expansion and saline contraction coefficients, respectively. The value of α significantly increases with temperature and β is almost uniform within the parameter range of the upper ocean in the KOCR (Gill, 1982; Jing et al., 2019). By converting SST and SSS differences into SSD using spatially constant α and β, we can estimate the impact of the background SST distribution (here we choose $\alpha = 0.22$ kg °C^{-1} m^{-3} and $\beta = 0.77$ kg psu^{-1} m^{-3}). Figs. 9f-h show the SSD anomalies estimated through a linear relationship between temperature, salinity, and potential density. The negative values of the SSD differences under the linear relation (Fig. 9h) extend more poleward than those of the actual SSD differences (Fig. 9e), primarily due to larger contributions from SST (Figs. 9c, f). Similar patterns but weaker magnitudes are also evident in composites from the FORA-WNP30, again confirming the importance of nonlinearity in generating SSD anomalies. We note that a recent study demonstrated that differences in the thermohaline properties of mesoscale eddies in the KE and those in the Oyashio region can also be explained by the meridional contrasts in the thermal expansion coefficients associated with the front of background SST (Jing et al., 2019).

Changes in SSD can alter the density stratification, hence affecting the MLD, which is an important parameter for controlling the effective heat capacity of the upper ocean. To assess the impacts of temperature and salinity variations on the MLD, we also decompose the MLD differences between the positive and negative years using the method described above. Here, the MLD is defined as a depth at which the density increases by 0.125 kg m^{-3} over the SSD.

The total differences in MLD in the KOCR are characterized by a complex spatial pattern with meridionally alternating positive and negative anomalies (Fig. 9k). During the positive year, a significant ML shoaling is observed around 38–40°N and 32–35°N, whereas deepening of ML is observed to north of 40°N. Distinct MLD variations associated with changes in the dynamical state of the KE are also pointed out by Oka et al. (2012); they have found that deepening of wintertime ML is observed around 31–35°N and 40–42°N during a stable state of KE (see their Fig. 4). Given that a positive (negative) year generally corresponds to an unstable (a stable) state of KE, our results are fairly consistent with findings of Oka et al, (2012), although some discrepancies are found in the details of their spatial patterns, arguably due to differences in data period and processing methods.

A decomposition of these differences demonstrates that the ML shoaling in the KOCR during positive years is limited to the south of 40°N because of the salinity effects (Fig. 9j). This can be explained by an anomalous increase in SSD near the surface associated with positive SSS anomalies there (Figs. 9b, d). Meanwhile, contributions from temperature anomalies dominate those of salinity anomalies to the south (Fig. 9i). Again, the qualitatively same features were found in composites from the FORA-WNP30 (Figs. 10i–k), but the ML shoaling in the southern KOCR was also caused by salinity anomalies (around 36°–38°N). Such MLD changes cannot be simply explained by corresponding SSD anomalies, implying that subsurface salinity anomalies also play an important role in determining the distribution of MLD.

To highlight the vertical structure of the temperature and salinity contributions to density anomalies, we constructed depth-latitude sections of the decomposed anomalies (Figs. 11 and

12). The anomalous high temperature and salinity near the climatological thermohaline fronts (Figs. 11a, b) have their peak near the surface (thermocline depth) in the northern (southern) part of the KOCR. These positive temperature and salinity anomalies generate offsetting density perturbations (Figs. 11c, d).

Due to the larger thermal expansion coefficients for warmer water, the contributions from temperature dominate the total density field to the south of 38°N, but they become comparable (~80% of temperature's contribution; figure not shown) to those of salinity to the north (Fig. 11e). The effects of these anomalies on the density stratification can be inferred from the composite of squared buoyancy frequency $N^2(z) = \frac{-g}{\rho_0}\frac{\partial \rho}{\partial z}$ (Figs. 11f–h). Here, we have computed $N^2(z)$ from the density field using the central difference scheme with a uniform vertical grid. For the poleward side of the KOCR (north of 38°N), positive differences in $N^2(z)$ (i.e., strengthening of the stratification) due to anomalous surface warming (Fig. 11f) were significantly compensated by concomitant increase in salinity and potential density near the surface (Fig. 11g). For the southern side, by contrast, salinity effects are not so large and total differences largely reflect contributions from temperature (Figs. 11f, h). A similar meridional contrast of hydrographic structures can also be seen in the composites from the FORA-WNP30 (Fig. 12), although subsurface differences around the KE latitude (~36°–38°N) are more prominent compared to the Argo data. Both in the Argo and FORA-WNP30 products, salinity variations in the KOCR have nonnegligible contributions to the density perturbations compared to temperature variations, and they become comparable to those of temperature to the north of 38°N as the background temperature decreases poleward. Therefore, these salinity variations have the potential to significantly affect the strength of the vertical mixing and evolution of temperature, which will be carefully quantified in the next section using the 1-D ML model experiments.

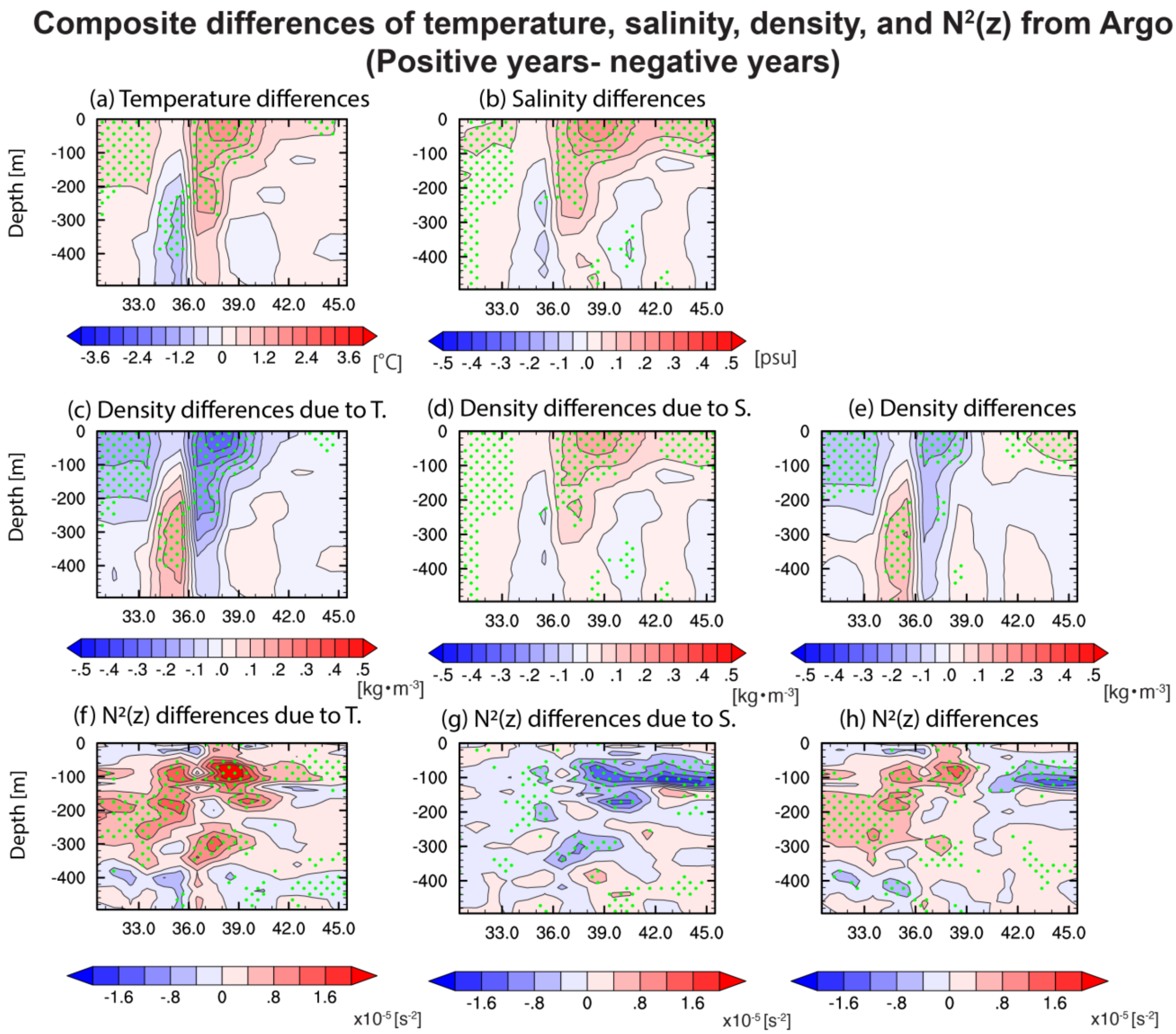

Figure 11. (a): Latitude-depth section of composited temperature differences between positive and negative years during February-April from the Argo data (in °C). The contour intervals are 0.4. (b): As in (a), but for salinity differences (in psu). The contour intervals are 0.05. (c)–(e): As in (a) and (b), but for (e) density

differences and contribution from (c) temperature and (d) salinity differences (in kg m^{-3}). The contour intervals are 0.05. (f)–(h): As in (c)–(e), but for the squared buoyancy frequency anomalies (in s^{-2}). The contour intervals are $4{\times}10^{-6}$. The differences that are significant at the 80% confidence levels on the basis of a two-tailed t-test are green dotted.

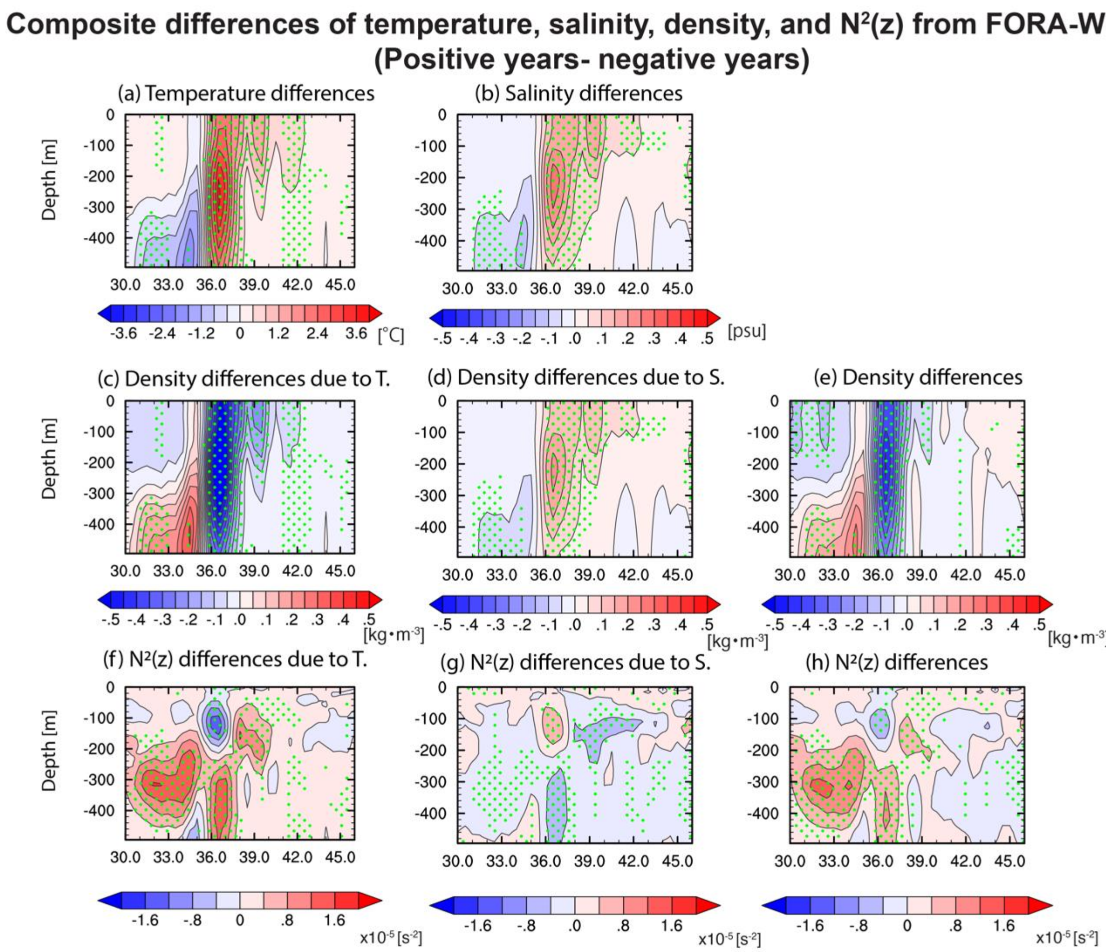

Figure 12. As in Fig. 11, but from the FORA-WNP30.

4.2 Quantitative assessment using 1-D model

Before proceeding to sensitivity experiments of the 1-D ML model, we first check the performance of our control (CTL) experiment, which is a reference for the sensitivity experiments. In the CTL experiment, the model is driven by atmospheric forcing from the J-OFURO3, geostrophic current fields from the FORA-WNP30, and temperature and momentum dynamical correction terms derived from the preliminary experiment, whereas the modeled salinity is strongly nudged toward the values of the FORA-WNP30, as detailed in Section 2.2. Owing to the implementation of the dynamical correction methods, the model aptly captures the spatial pattern of the climatological SST and SSS fields (Figs. 13a–f), although the modeled SST is slightly warmer (cooler) to the north (south) of 40°N compared to that of the FORA-WNP30. Here, we have shown the wintertime mean state as a representative period with strong SST/SSS fronts; however, the climatology of other seasons, such as the March–May averaged field, is also simulated well by the 1-D model. In addition, the climatology of the subsurface temperature and salinity fields, as well as the horizontal currents, is also in good agreement with the reanalysis product (figures not shown). This suggests that our 1-D model can adequately simulate the background oceanic conditions over the western North Pacific. Furthermore, the time evolutions of area-averaged SST anomalies over the KOCR from the FORA-WNP30 and the 1-D model are also compared well (Fig. 13g). Similarly, the SSS variation in the 1-D model also corresponds well with that in the reanalysis product (Fig. 13h), as was expected from the adoption of salinity nudging during the CTL experiment. These conspicuous agreements between the 1-D ML model and the reanalysis product allow us to make further use of it for a more detailed investigation.

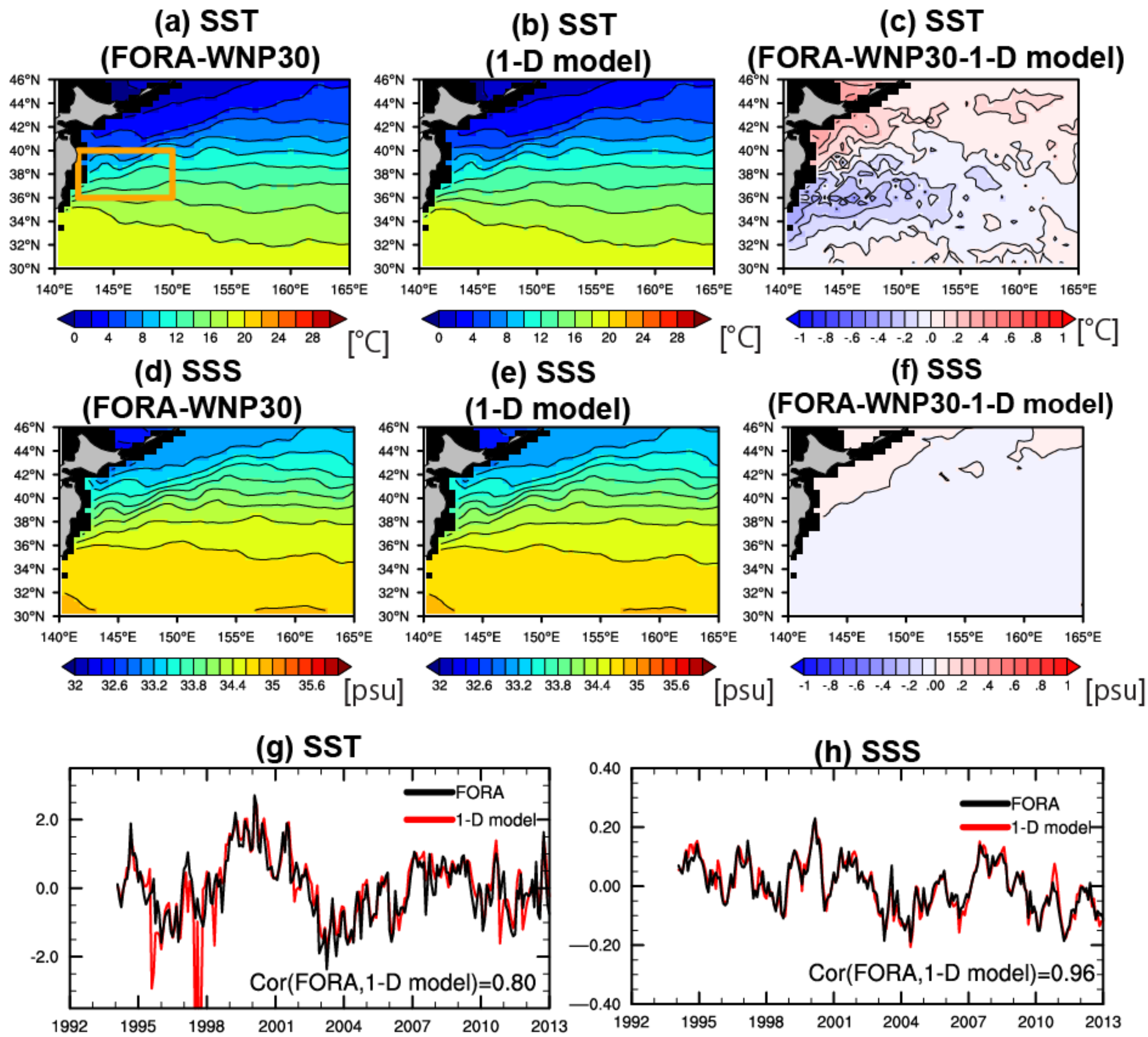

Figure 13. (a), (b): Climatological SST during January–March from (a) the FORA-WNP30 and (b) the CTL experiment of the 1-D ML model (in °C). The differences between (a) and (b) are shown in (c). The contour intervals in (a) and (b) are 2, whereas those in (c) are 0.1. (d)–(f): As in (a)–(c), but for SSS (in psu). The contour intervals in (d) and (e) are 0.2, whereas those in (f) are 0.1. (g): Time series of area-averaged SST anomalies over the KOCR (see the orange box in (a)) from the

FORA-WNP30 (black) and 1-D ML model (red). The correlation coefficient between them is shown in the lower right. (h) As in (g), but for SSS anomalies.

While both temperature and salinity variability are dominated by the same 3-D mechanisms as discussed above, here we intend to clarify how and to what extent salinity has potential to modify dynamical and thermodynamical processes in the upper ocean. Motivated by the fact that many previous studies on the KOCR have not explicitly considered the salinity effects mainly due to limited salinity observations, we explore this issue with an artificial experiment with the 1-D model. To explicitly depict the role played by salinity variability, we treat salinity as a "forcing" in the 1-D ML model and see "responses" of other related variables, such as the vertical diffusion coefficients and temperature. Based on this concept, we have designed another set of experiments that nullify the salinity's roles by artificially suppressing its fluctuation (referred to as the climatological salinity (Sclim) experiment). In this experiment, we initialize and force the model as in the CTL experiment, except that salinity used for the initial and restoring conditions was replaced by corresponding climatological values. With sufficiently strong relaxation, salinity variations (except for the seasonal cycle) and associated changes in density stratification and related processes are eliminated. As the same temperature and momentum dynamical correction were used in both the CTL and Sclim experiments, the collective impacts of salinity anomalies on the vertical mixing process and associated changes in temperature can be adequately measured by considering difference between the CTL and Sclim experiments (Kido & Tozuka, 2017). This framework provides useful insights regarding the significance of salinity effects, although it has an inevitable limitation due to its absence of three-dimensional responses (e.g., possible changes in temperature advection associated with salinity-induced current anomalies are not included). Because oceanic anomalies during negative years are close to a mirror image of those during positive years, we only conducted the Sclim experiment for the seven positive years appeared in the FORA-WNP30 (see Table 1).

The observed anomalous surface warming and saltening over the KOCR during the late winter to spring of the positive years (Figs. 14a, b) were well reproduced in the CTL experiment (Figs. 14c, d), further confirming its satisfactory ability to simulate the observed variability. To isolate the effects of salinity anomalies, we calculated the differences in the SST and SSS fields between the CTL and Sclim experiments for all selected positive years and their composites, as shown in Figs. 14e, f. The spatial pattern of the SSS differences between the two experiments (Fig. 14f) closely resembles the composite SSS anomalies (Fig. 14d; see also Figs. 3f and 4f), suggesting that the targeted SSS anomalies over the KOCR were successfully removed in the Sclim experiment. The SST differences were characterized by negative (positive) values over the northern (southern) part of the KOCR, suggesting that the inclusion of salinity anomalies during positive years led to cooling (warming) in those parts (Fig. 14e). This implies that salinity variations during the positive years serve to dampen (amplify) the concomitant SST warming over the northern (southern) part of the KOCR and hence, inhibit the poleward intrusion of anomalous warming. The areas with cooler (warmer) SST in the CTL than the Sclim experiment roughly coincide with the regions where salinity anomalies contribute to the weakening (strengthening) of density stratification and deepening (shoaling) of the mixed layer, indicating that changes in the vertical process may hold the key. These differences are commonly seen in all positive years and the maximum differences in SST between the two experiments reaches 1.0°C, which constitutes 20%–40% of the total SST anomalies there (Figs. 14c, e). Therefore, salinity variations in the KOCR can exert significant effects on the evolution of SST therein by modulating the 1-D vertical process.

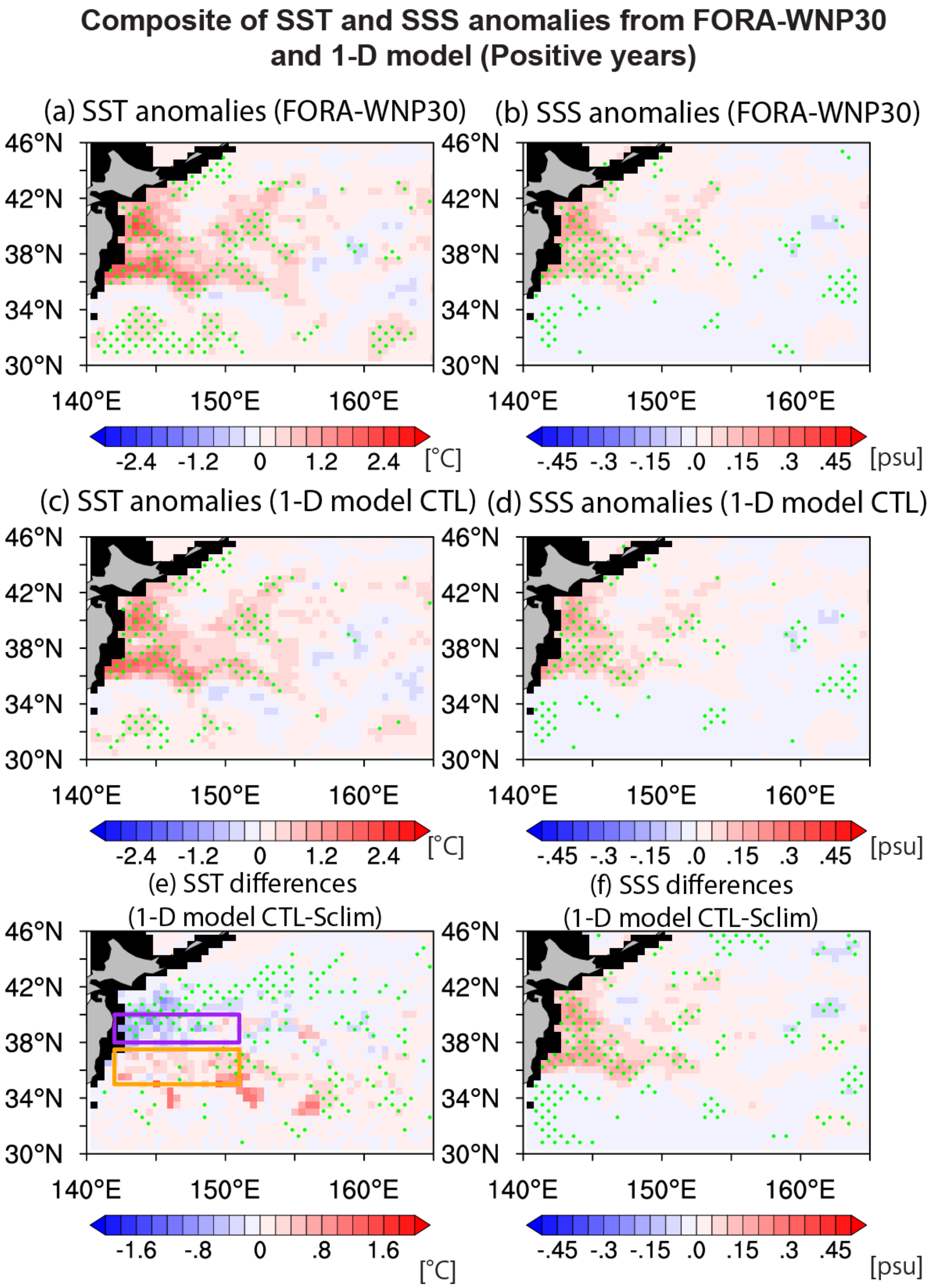

Figure 14. (a), (b): Composite of (a) SST (in °C) and (b) SSS (in psu) anomalies during February-April during positive years from the FORA-WNP30. (c), (d): As in (a) and (b), but from the CTL experiment of the 1-D ML model. (e), (f): Composite of the difference in SST (e) and SSS (f) between the CTL and Sclim experiments of the 1-D ML model during March–May. The green dotted regions indicate differences that are significant at the 80% confidence levels on the basis of a two-tailed t test. The purple and orange boxes in (e) denote the northern and southern box, respectively.

What causes such distinct SST differences between the two experiments? Given the configurations of our 1-D ML model experiments, there are two possible explanations for these differences. First, changes in the MLD due to salinity anomalies (cf. Figs. 9i–k and 10i–k) can alter the effective heat capacity of the upper ocean and affect the sensitivity of SST to atmospheric heat flux. Second, changes in vertical stratification due to salinity anomalies may modulate the strength of vertical mixing and turbulent heat transport in the upper ocean. To assess the first hypothesis, we carried out a detailed mixed layer heat budget analysis based on the output from the 1-D ML model (see the supplementary material for details), and it was found that the MLD changes due to salinity anomalies have the opposite effect. These results indicate that the SST differences between the two experiments cannot be simply explained by those in the atmospheric heat flux or MLD, implying that modulations in vertical mixing and associated heat transport hold the key.

To confirm the above statement and further illuminate the related physical processes, we next check the time evolution of other mixing-related parameters, such as the density stratification and vertical mixing coefficient from each experiment. The time-depth plots of the area-averaged composited temperature, salinity, squared buoyancy frequency ($N^2(z)$), and vertical diffusion coefficient of temperature (κ_T: see Eq. 1) from both 1-D ML model experiments are shown in Figs. 15 (the northern box) and 16 (the southern box).

For the northern box, the seasonal cycle of temperature and salinity variation, such as the gradual deepening of the mixed layer in winter and rapid shoaling during spring, are reproduced in both experiments, (Figs. 15a, b, d, e). Differences between the CTL and Sclim experiments demonstrate that the positive salinity anomalies near the surface begin to develop in winter, peak in spring, and subsequently decay in summer (Fig. 15f). These salinity anomalies serve to weaken upper ocean stratification at 100–150 m depth (Fig. 15i) and then lead to the strengthening of the vertical mixing there (Fig. 15l). As a result, the vertical heat exchange between the surface and subsurface layer during late winter to early spring is greatly enhanced, giving rise to cooler SST and a warmer subsurface temperature in the CTL experiment (Fig. 15c), supporting the hypothesis proposed above. We again note that temperature differences between the CTL and Sclim experiments are caused only by changes in the vertical diffusion because both experiments adopt the same amount of dynamical corrections and shortwave radiation. Thus, the chain of physical processes described above is adequately represented in our experimental framework. The maximum SST differences were found during April–May and then subducted below the seasonal thermocline during summer and fall. Differences in the subsurface temperature (i.e., warmer temperatures in the CTL experiment) at 150–200 m depth also persist through summer and remain until fall, even though no salinity signals survive until this season.

Therefore, the salinity-induced temperature perturbations can persist longer than the salinity variations themselves and hence have the potential to affect the low-frequency variation of upper ocean.

The 1-D ML model also satisfactorily reproduces the key features of temperature and salinity variation within the southern box (Figs. 16a–f), as in the northern box. Significant positive salinity signals are also evident in the difference between the two experiments, but their maximum peak is found at 100–150 m depth rather than near the surface (Figs. 16d–f). Consequently, the density stratification is strengthened (Fig. 16i) and vertical mixing near the thermocline is substantially more suppressed in the CTL experiment than in the Sclim experiment (Fig. 16l). Therefore, the vertical entrainment of subsurface cold water is significantly reduced, and eventually leads to a warmer SST (and slightly lower thermocline temperature) in the CTL experiment.

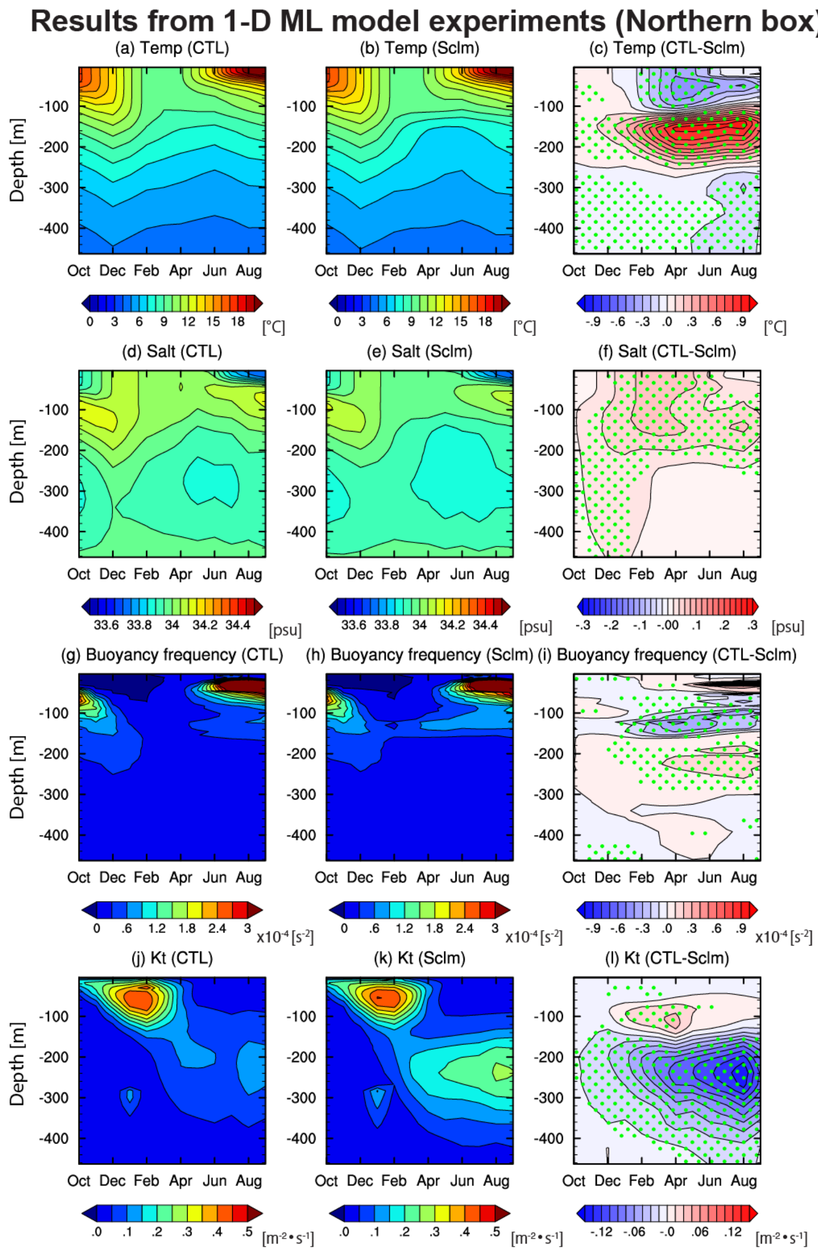

Figure 15. (a)–(c): Time evolution of composited temperature in (a) CTL and (b) Sclim experiments during positive years (in °C), and (c) their difference (i.e., CTL minus the Sclim experiments) averaged over the northern box (142°E-151°E, 38°N-40°N: See the purple box in Fig. 14e). The contour intervals in (a) and (b) are 1, whereas those in (c) are 0.1. The differences that are significant at the 80%

confidence levels on the basis of a two-tailed t-test are green dotted in (c). (d)–(f): As in (a)–(c), but for salinity (in psu). The contour intervals in (d) and (e) are 0.05, whereas those in (f) are 0.03. (g)–(i): As in (a)–(c), but for the squared buoyancy frequency (in s^{-2}). The contour intervals are 3×10^{-5}. (j)–(l): As in (a)–(c), but for the vertical diffusion coefficients (in $m^2\ s^{-1}$). The contour intervals are 5×10^{-2}.

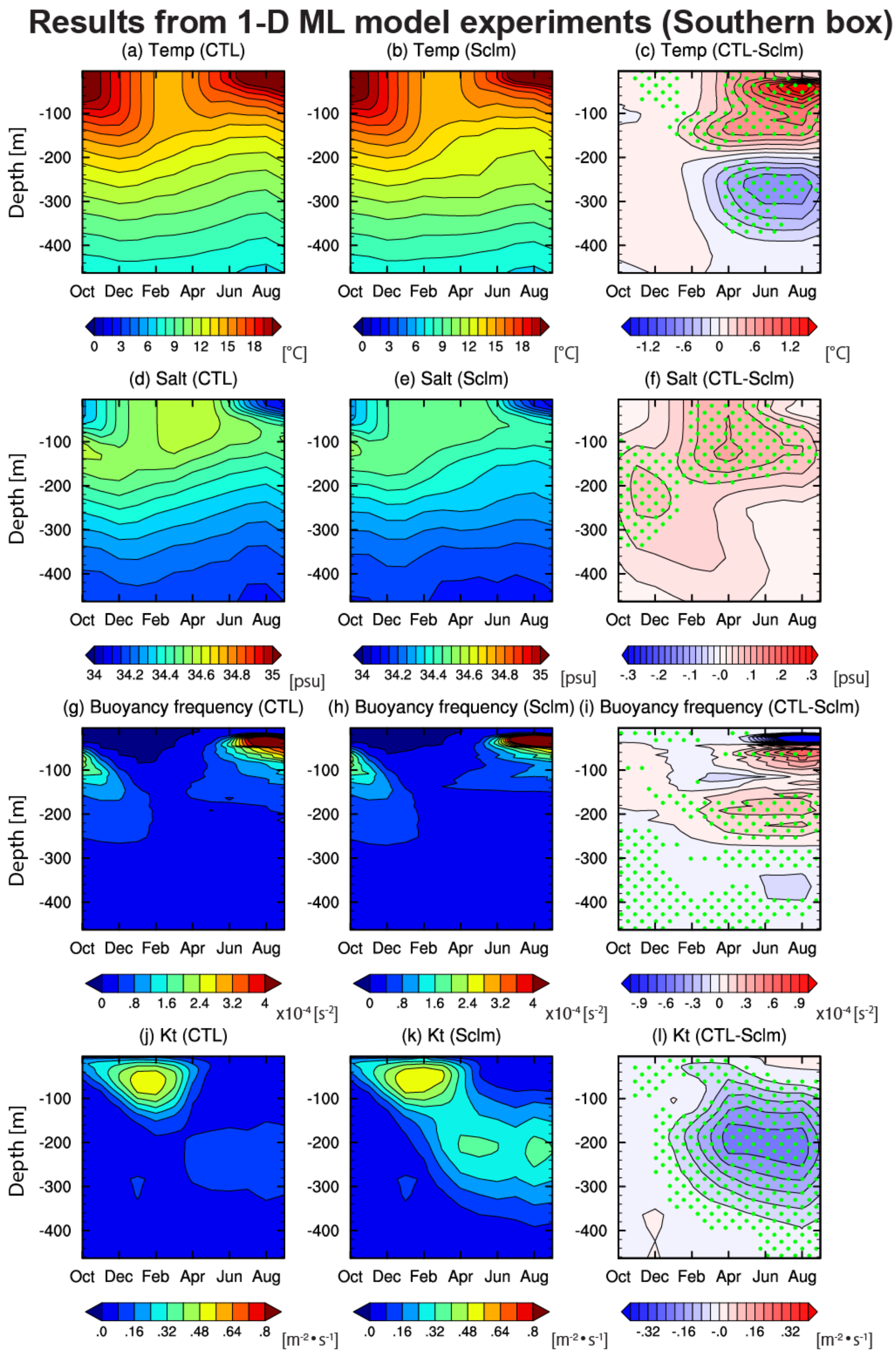

Figure 16. As in Fig. 15, but for the southern box (142°E-151°E, 35°N-37°N: See the purple box in Fig. 14e).

5. Summary and discussion

Using observational datasets and an eddy-resolving ocean reanalysis product (FORA-WNP30), in this study, we investigated low-frequency variations of upper ocean salinity in the KOCR and examined their mechanism and possible effects on the mixed-layer processes, with a specific focus on variability during the boreal winter to spring. From a gridded dataset based on the Argo profiles and an eddy-resolving ocean reanalysis product, we identified a coherent interannual to decadal variation in temperature and salinity in the KOCR, with anomalous saltening (freshening) tending to be accompanied by significant warming (cooling) across the same region. Based on the area-averaged SST and SSS anomalies in the KOCR, we selected several typical years for such events, and a positive (negative) year is defined as one with a significant increase (decrease) in both SST and SSS in the area. A close inspection of the three-dimensional structures of composite temperature and salinity anomalies reveals that such anomalies are concentrated near the surface in the northern part of the KOCR, but strong anomalies are found at 200–400 m depth in the southern part of the KOCR. Such meridional differences in the vertical structures of thermohaline anomalies reflect the distribution of the climatological temperature and salinity fronts, which was also pointed out by earlier works (Nakamura & Kazmin, 2003; Nonaka et al., 2006).

The mechanisms of these salinity variations were then explored based on the basis of a composite and lag correlation analysis of the related physical variables. We found that the dynamical stability of the KE was the predominant factor behind the observed variations. During positive years, accompanying an unstable state of the KE, an increase in the SSH and anomalous anticyclonic circulation could be observed in the northern part of the KE. Further, associated northeastward current anomalies directing toward the KOCR enhanced the poleward transport of warm and saline water originating from the subtropics, leading to significant surface warming and saltening in the KOCR. At the same time, the intensification of mesoscale eddy activity and eddy-induced advection in the upstream of the KE also contribute to the generation of positive temperature and salinity anomalies in the KOCR. The increase in surface evaporation due to positive SST anomalies also serves to maintain the positive SSS in the KOCR, but its contribution is relatively small compared to the ocean dynamical effects mentioned above. Similar anomalies, but with opposite polarities (i.e., features with a stable state of the KE) also contribute to anomalous cooling and freshening during negative years.

To quantify the effects of these salinity variations on the density of seawater and vertical stratification, we decomposed the density anomalies into contributions from temperature and salinity anomalies. During the positive years, positive SSS anomalies in the northern part of the KOCR lead to an increase in surface density and serve to deepen the mixed layer in that region. Similarly, the positive subsurface salinity anomalies in the southern part of the KOCR enhance the vertical stability and contribute to the shoaling of the mixed layer by increasing the density at that depth. These salinity-induced density perturbations compensate for the concomitant temperature-induced density perturbations and significantly reduce the amplitude of total anomalies. Salinity contributions to density anomalies increase poleward and become comparable to those of temperature in the northern part of the KOCR, and this can be explained by the weaker dependence of density on temperature due to lower background temperatures in that region. These results suggest that salinity variations in the KOCR have substantial impacts on the local density fields and may exert considerable effects on dynamical and thermodynamical processes.

Based on the results from the density decomposition, we have assessed the impacts of the density changes associated with salinity anomalies upon the strength of vertical mixing and evolution of the upper ocean temperature by carefully designing and conducting a series of sensitivity experiments using the 1-D ML model. These sensitivity experiments demonstrated that salinity anomalies during positive years serve to cool SST in the northern part of the KOCR by up to −1.0°C, whereas in the southern part, they cause SST warming of the same amplitude. By analyzing other variables from the 1-D ML model, it was found that changes in density stratification due to salinity anomalies indeed modulate the strength of vertical mixing and induce significant responses in the upper ocean temperature. More specifically, positive SSS anomalies in the northern part of the KOCR reduce the density stratification and strengthen the vertical mixing in that region, resulting in significant near surface cooling and subsurface warming in that region. In the southern part, by contrast, positive subsurface salinity anomalies during positive years stabilize the upper ocean column and suppress the vertical exchange of heat within the mixed layer, leading to near surface warming and (weaker) subsurface cooling. Thus, surface and subsurface salinity anomalies in the KOCR suppress the poleward expansions of co-occurring temperature anomalies.

The close linkage between the dynamical states of the KE and SST variations over the KOCR has been documented in several previous studies (Masunaga et al., 2016; Qiu et al., 2017; Sasaki & Minobe, 2015; Sugimoto et al., 2014). However, little has been discovered concerning the concomitant salinity variations and associated mechanisms. In this regard, we have shown, primarily based on a lagged correlation analysis, that ocean dynamical processes, especially the modulation of heat and salt transport by large-scale circulation and mesoscale eddies, are closely related to the wintertime temperature and salinity variations in the KOCR. Although these conclusions are physically consistent and in accordance with many previous studies, they are still based on statistical relationships and more physical approaches are required to confirm their validity. An accurate salinity budget analysis as well as coordinated sensitivity experiments using high-resolution ocean general circulation models (OGCMs) would be helpful in addressing these issues.

In this study, we demonstrated that salinity has the potential to play an active role in low-frequency variations in the KOCR by modulating the upper ocean temperature via density change. These results have important implications for the study of climate variability in the North Pacific, as the SST variability in the KOCR affects atmospheric circulation, as discussed in Section 1 (Frankignoul et al., 2011; Taguchi et al., 2012). Due to the strong internal variability of the atmosphere and ocean, how and to what extent these atmospheric responses to SST anomalies feed back onto the ocean is still a matter for debate, but salinity may be involved in such feedback processes, provided that it exerts strong impacts on SST. An important caveat of this study is that our estimates of salinity impacts on SST based on the 1-D ML model disregard changes in three-dimensional advective processes produced by salinity anomalies. As salinity anomalies may also alter circulation in the upper ocean and the associated transport of heat and momentum, well-designed OGCM and data assimilation experiments are necessary to incorporate and assess the significance of such effects. Finally, strong salinity fronts are also found in other WBCs such as the Gulf Stream, Agulhas Current, and Antarctic Circumpolar Current (Kida et al., 2015; Ohishi et al., 2019), and similar salinity variations may also be evident in these regions. The applications of our approach to other WBCs and comparisons to the KOCR results will provide further insight into the physical processes operating in the WBCs and their roles in midlatitude climate variability.

Acknowledgments

We would like to thank Tomoki Tozuka, Eitarou Oka, and Shota Katsura for their insightful comments and suggestions, and Norihisa Usui for his technical advice on the use of FORA- Constructive comments from two anonymous reviewers have significantly improved an early version of the manuscript. Data used were obtained as follows; the gridded Argo product from the Scripps Institution of Oceanography is from http://sio-argo.ucsd.edu/RG_Climatology.html; the FORA-WNP30 data is from http://synthesis.jamstec.go.jp/FORA/e/index.html; and the J-OFURO3 surface flux data is from https://j-ofuro.isee.nagoya-u.ac.jp/en/. The present study is supported by KAKENHI JP19H05701, JP19H05702, JP18H03726, and 21K13997.

References

Dong, D., Brandt, P., Chang, P., Schütte, F., Yang, X., Yan, J., & Zeng, J. (2017). Mesoscale eddies in the northwestern Pacific Ocean: Three-dimensional eddy structures and heat/salt transports. *Journal of Geophysical Research: Oceans*, *122*(12), 9795–9813. https://doi.org/10.1002/2017JC013303

Duchon, C. E. (1979). Lanczos filtering in one and two dimensions. *Journal of Applied Meteorology*, *18*(8), 1016–1022. https://doi.org/10.1175/1520-0450(1979)018<1016:LFIOAT>2.0.CO;2

Frankignoul, C., Sennéchael, N., Kwon, Y.-O., & Alexander, M. A. (2011). Influence of the meridional shifts of the Kuroshio and the Oyashio Extensions on the atmospheric circulation. *Journal of Climate*, *24*(3), 762–777. https://doi.org/10.1175/2010JCLI3731.1

Furuichi, N., Hibiya, T., & Niwa, Y. (2012). Assessment of turbulence closure models for resonant inertial response in the oceanic mixed layer using a large eddy simulation model. *Journal of Oceanography*, *68*(2), 285–294. https://doi.org/10.1007/s10872-011-0095-3

Geng, Y., Wang, Q., & Mu, M. (2018). Effect of the Decadal Kuroshio Extension Variability on the Seasonal Changes of the Mixed-Layer Salinity Anomalies in the Kuroshio-Oyashio Confluence Region. *Journal of Geophysical Research: Oceans*, *123*(12), 8849–8861. https://doi.org/10.1029/2018JC014139

Gill, A. E. (1982). *Atmosphere Ocean dynamics* (Internatio). Academic Press.

Hasson, A. E. A., Delcroix, T., & Dussin, R. (2013). An assessment of the mixed layer salinity budget in the tropical Pacific Ocean. Observations and modelling (1990-2009). *Ocean Dynamics*, *63*(2–3), 179–194. https://doi.org/10.1007/s10236-013-0596-2

Hosoda, S., Ohira, T., & Nakamura, T. (2008). A monthly mean dataset of global oceanic temperature and salinity derived from Argo float observations. *JAMSTEC Report of Research and Development*, *8*(November), 47–59. https://doi.org/10.5918/jamstecr.8.47

Isoguchi, O., Kawamura, H., & Oka, E. (2006). Quasi-stationary jets transporting surface warm waters across the transition zone between the subtropical and the subarctic gyres in the North Pacific. *Journal of Geophysical Research*, *111*(C10), C10003. https://doi.org/10.1029/2005JC003402

Itoh, S., & Yasuda, I. (2010). Characteristics of mesoscale eddies in the Kuroshio–Oyashio extension region detected from the distribution of the sea surface height anomaly. *Journal* *of Physical Oceanography*, *40*(5), 1018–1034. https://doi.org/10.1175/2009JPO4265.1

Jackett, D. R., & Mcdougall, T. J. (1995). Minimal Adjustment of Hydrographic Profiles to Achieve Static Stability. *Journal of Atmospheric and Oceanic Technology*. https://doi.org/10.1175/1520-0426(1995)012<0381:maohpt>2.0.co;2

Jing, Z., Chang, P., Shan, X., Wang, S., Wu, L., & Kurian, J. (2019). Mesoscale SST dynamics in the Kuroshio-Oyashio extension region. *Journal of Physical Oceanography*, *49*(5), 1339–1352. https://doi.org/10.1175/JPO-D-18-0159.1

Kara, A. B., Hurlburt, H. E., & Wallcraft, A. J. (2005). Stability-dependent exchange coefficients for air-sea fluxes. *Journal of Atmospheric and Oceanic Technology*, *22*(7), 1080–1094. https://doi.org/10.1175/JTECH1747.1

Kelly, K. A., Small, R. J., Samelson, R. M., Qiu, B., Joyce, T. M., Kwon, Y.-O., & Cronin, M. F. (2010). Western boundary currents and frontal air-sea interaction: Gulf stream and Kuroshio Extension. *Journal of Climate*, *23*(21), 5644–5667. https://doi.org/10.1175/2010JCLI3346.1

Kida, S., Mitsudera, H., Aoki, S., Guo, X., Ito, S. ichi, Kobashi, F., et al. (2015). Oceanic fronts and jets around Japan: a review. *Journal of Oceanography*, *71*(5), 469–497. https://doi.org/10.1007/s10872-015-0283-7

Kido, S., & Tozuka, T. (2017). Salinity variability associated with the positive Indian Ocean Dipole and its impact on the upper ocean temperature. *Journal of Climate*, *30*(19), 7885–7907. https://doi.org/10.1175/JCLI-D-17-0133.1

Kido, S., Tozuka, T., & Han, W. (2019a). Anatomy of salinity anomalies associated with the positive Indian Ocean Dipole. *Journal of Geophysical Research: Oceans*, *124*(11), 8116–8139. https://doi.org/10.1029/2019JC015163

Kido, S., Tozuka, T., & Han, W. (2019b). Experimental assessments on impacts of salinity anomalies on the positive Indian Ocean Dipole. *Journal of Geophysical Research: Oceans*, *124*(12), 9462–9486. https://doi.org/10.1029/2019JC015479

Kitamura, T., Nakano, T., & Sugimoto, S. (2016). Decadal variations in mixed layer salinity in the Kuroshio Extension recirculation gyre region: influence of precipitation during the warm season. *Journal of Oceanography*. https://doi.org/10.1007/s10872-015-0317-1

Kobayashi, S., Ota, Y., Harada, Y., Ebita, A., Moriya, M., Onoda, H., et al. (2015). The JRA-55 Reanalysis: General Specifications and Basic Characteristics. *Journal of the Meteorological Society of Japan. Ser. II*, *93*(1), 5–48. https://doi.org/10.2151/jmsj.2015-001

Kwon, Y.-O., & Deser, C. (2007). North Pacific decadal variability in the community climate system model version 2. *Journal of Climate*, *20*(11), 2416–2433. https://doi.org/10.1175/JCLI4103.1

Kwon, Y.-O., Alexander, M. A., Bond, N. A., Frankignoul, C., Nakamura, H., Qiu, B., & Thompson, L. A. (2010). Role of the Gulf Stream and Kuroshio-Oyashio systems in large-scale atmosphere-ocean interaction: A review. *Journal of Climate*, *23*(12), 3249–3281. https://doi.org/10.1175/2010JCLI3343.1

Li, J., Liang, C., Tang, Y., Liu, X., Lian, T., Shen, Z., & Li, X. (2018). Impacts of the IOD-associated temperature and salinity anomalies on the intermittent equatorial undercurrent anomalies. *Climate Dynamics, 51*(4), 1391–1409. https://doi.org/10.1007/s00382-017-3961-x

Ma, X., Chang, P., Saravanan, R., Montuoro, R., Hsieh, J. S., Wu, D., et al. (2015). Distant Influence of Kuroshio Eddies on North Pacific Weather Patterns? *Scientific Reports, 5,* 1–7. https://doi.org/10.1038/srep17785

Masunaga, R., Nakamura, H., Miyasaka, T., Nishii, K., & Qiu, B. (2016). Interannual modulations of oceanic imprints on the wintertime atmospheric boundary layer under the changing dynamical regimes of the Kuroshio Extension. *Journal of Climate, 29*(9), 3273–3296. https://doi.org/10.1175/JCLI-D-15-0545.1

Masuzawa, J. (1969). Subtropical mode water. *Deep Sea Research and Oceanographic Abstracts, 16*(5), 463–472. https://doi.org/10.1016/0011-7471(69)90034-5

Nagano, A., Uehara, K., Suga, T., Kawai, Y., Ichikawa, H., & Cronin, M. F. (2014). Origin of near-surface high-salinity water observed in the Kuroshio Extension region. *Journal of Oceanography*, *70*(4), 389–403. https://doi.org/10.1007/s10872-014-0237-5

Nakamura, H., & Kazmin, A. S. (2003). Decadal changes in the North Pacific oceanic frontal zones as revealed in ship and satellite observations. *Journal of Geophysical Research, 108*(C3), 3078. https://doi.org/10.1029/1999JC000085

Nakamura, H., Lin, G., & Yamagata, T. (1997). Decadal Climate Variability in the North Pacific during the Recent Decades. *Bulletin of the American Meteorological Society*, *78*(10), 2215–2225. https://doi.org/10.1175/1520-0477(1997)078<2215:DCVITN>2.0.CO;2

Nakamura, H., Sampe, T., Tanimoto, Y., & Shimpo, A. (2004). Observed associations among storm tracks, jet streams and midlatitude oceanic fronts. *Geophysical Monograph Series*, *147*, 329–345. https://doi.org/10.1029/147GM18

Nan, F., Yu, F., Xue, H., Wang, R., & Si, G. (2015). Ocean salinity changes in the northwest Pacific subtropical gyre: The quasi-decadal oscillation and the freshening trend. *Journal of Geophysical Research: Oceans*, *120*(3), 2179–2192. https://doi.org/10.1002/2014JC010536

Nonaka, M., Nakamura, H., Tanimoto, Y., Kagimoto, T., & Sasaki, H. (2006). Decadal variability in the Kuroshio–Oyashio extension simulated in an eddy-resolving OGCM. *Journal of Climate*, *19*(10), 1970–1989. https://doi.org/10.1175/JCLI3793.1

Nonaka, M., Nakamura, H., Tanimoto, Y., & Sasaki, H. (2008). Interannual-to-decadal variability in the Oyashio and its influence on temperature in the subarctic frontal zone: An eddy-resolving OGCM simulation. *Journal of Climate*, *21*(23), 6283–6303. https://doi.org/10.1175/2008JCLI2294.1

Nonaka, M., Sasaki, H., Taguchi, B., & Nakamura, H. (2012). Potential predictability of interannual variability in the Kuroshio extension jet speed in an eddy-resolving OGCM. *Journal of Climate*, *25*(10), 3645–3652. https://doi.org/10.1175/JCLI-D-11-00641.1

Nonaka, M., Sasai, Y., Sasaki, H., Taguchi, B., & Nakamura, H. (2016). How potentially predictable are midlatitude ocean currents? *Scientific Reports*, *6*(August 2015), 1–8. https://doi.org/10.1038/srep20153

Nonaka, M., Sasaki, H., Taguchi, B., & Schneider, N. (2020). Atmospheric-Driven and Intrinsic Interannual-to-Decadal Variability in the Kuroshio Extension Jet and Eddy Activities. *Frontiers in Marine Science*. https://doi.org/10.3389/fmars.2020.547442

Ohishi, S., Katsura, S., & Aiki, H. (2019). Salinity frontogenesis/frontolysis in the northeastern subtropical Pacific region. *Climate Dynamics*, *53*(9–10), 5927–5943. https://doi.org/10.1007/s00382-019-04907-w

Oka, E., & Qiu, B. (2012). Progress of North Pacific mode water research in the past decade. *Journal of Oceanography*, *68*(1), 5–20. https://doi.org/10.1007/s10872-011-0032-5

Oka, E., Qiu, B., Kouketsu, S., Uehara, K., & Suga, T. (2012). Decadal seesaw of the Central and Subtropical Mode Water formation associated with the Kuroshio Extension variability. *Journal of Oceanography*, *68*(2), 355–360. https://doi.org/10.1007/s10872-011-0098-0

Pak, G., Park, Y.-H., Vivier, F., Bourdallé-Badie, R., Garric, G., & Chang, K.-I. (2017). Upper-ocean thermal variability controlled by ocean dynamics in the Kuroshio-Oyashio Extension region. *Journal of Geophysical Research: Oceans*, *122*(2), 1154–1176.

https://doi.org/10.1002/2016JC012076

Paulson, C. A., & Simpson, J. J. (1977). Irradiance measurements in the upper ocean. *Journal of Physical Oceanography*, *7*(6), 952–956. https://doi.org/10.1175/1520-0485(1977)007<0952:IMITUO>2.0.CO;2

Pierini, S. (2006). A Kuroshio extension system model study: Decadal chaotic self-sustained oscillations. *Journal of Physical Oceanography*, *36*(8), 1605–1625. https://doi.org/10.1175/JPO2931.1

Pierini, S., Dijkstra, H. A., & Riccio, A. (2009). A nonlinear theory of the Kuroshio extension bimodality. *Journal of Physical Oceanography*, *39*(9), 2212–2229. https://doi.org/10.1175/2009JPO4181.1

Qiu, B. (2000). Interannual Variability of the Kuroshio Extension System and Its Impact on the Wi ntertime SST Field. *Journal of Physical Oceanography*, *30*(6), 1486–1502. https://doi.org/10.1175/1520-0485(2000)030<1486:IVOTKE>2.0.CO;2

Qiu, B. (2002). The Kuroshio Extension system: Its large-scale variability and role in the midlatitude ocean-atmosphere interaction. *Journal of Oceanography*, *58*(1), 57–75. https://doi.org/10.1023/A:1015824717293

Qiu, B., & Chen, S. (2005). Variability of the Kuroshio Extension jet, recirculation gyre, and mesoscale eddies on decadal time scales. *Journal of Physical Oceanography*, *35*(11), 2090–2103. https://doi.org/10.1175/JPO2807.1

Qiu, B., & Chen, S. (2010). Eddy-mean flow interaction in the decadally modulating Kuroshio Extension system. *Deep Sea Research Part II: Topical Studies in Oceanography*, *57*(13–14), 1098–1110. https://doi.org/10.1016/j.dsr2.2008.11.036

Qiu, B., & Kelly, K. A. (1993). Upper-Ocean heat balance in the Kuroshio Extension region. *Journal of Physical Oceanography*, *23*(9), 2027–2041. https://doi.org/10.1175/1520-0485(1993)023<2027:UOHBIT>2.0.CO;2

Qiu, B., Chen, S., Hacker, P., Hogg, N. G., Jayne, S. R., & Sasaki, H. (2008). The Kuroshio Extension Northern recirculation gyre: Profiling float measurements and forcing mechanism. *Journal of Physical Oceanography*, *38*(8), 1764–1779. https://doi.org/10.1175/2008JPO3921.1

Qiu, B., Chen, S., & Schneider, N. (2017). Dynamical links between the decadal variability of the Oyashio and Kuroshio Extensions. *Journal of Climate*, *30*(23), 9591–9605.

https://doi.org/10.1175/JCLI-D-17-0397.1

Roden, G. I. (1972). Temperature and salinity fronts at the boundaries of the subarctic-subtropical transition zone in the western Pacific. *Journal of Geophysical Research*, *77*(36), 7175–7187. https://doi.org/10.1029/JC077i036p07175

Roemmich, D., & Gilson, J. (2009). The 2004-2008 mean and annual cycle of temperature, salinity, and steric height in the global ocean from the Argo Program. *Progress in Oceanography*, *82*(2), 81–100. https://doi.org/10.1016/j.pocean.2009.03.004

Saito, H., Suga, T., Hanawa, K., & Watanabe, T. (2007). New type of pycnostad in the western subtropical-subarctic transition region of the North Pacific: Transition Region Mode Water. *Journal of Oceanography*, *63*(4), 589–600. https://doi.org/10.1007/s10872-007-0052-3

Sasaki, Y. N., & Minobe, S. (2015). Climatological mean features and interannual to decadal variability of ring formations in the Kuroshio Extension region. *Journal of Oceanography*, *71*(5), 499–509. https://doi.org/10.1007/s10872-014-0270-4

Schneider, N., Miller, A. J., & Pierce, D. W. (2002). Anatomy of North Pacific decadal variability. *Journal of Climate*, *15*(6), 586–605. https://doi.org/10.1175/1520-0442(2002)015<0586:AONPDV>2.0.CO;2

Seager, R., Kushnir, Y., Naik, N. H., Cane, M. A., & Miller, J. (2001). Wind-driven shifts in the latitude of the Kuroshio–Oyashio extension and generation of SST anomalies on decadal timescales. *Journal of Climate*, *14*(22), 4249–4265. https://doi.org/10.1175/1520-0442(2001)014<4249:WDSITL>2.0.CO;2

Smirnov, D., Newman, M., Alexander, M. A., Kwon, Y. O., & Frankignoul, C. (2015). Investigating the local atmospheric response to a realistic shift in the Oyashio sea surface temperature front. *Journal of Climate*, *28*(3), 1126–1147. https://doi.org/10.1175/JCLI-D-14-00285.1

Suga, T., Takei, Y., & Hanawa, K. (1997). Thermostad distribution in the North Pacific subtropical gyre: The central mode water and the subtropical mode water. *Journal of Physical Oceanography*, *27*(1), 140–152. https://doi.org/10.1175/1520-0485(1997)027<0140:TDITNP>2.0.CO;2

Suga, T., Motoki, K., Aoki, Y., & Macdonald, A. M. (2004). The North Pacific climatology of winter mixed layer and mode Waters. *Journal of Physical Oceanography*, *34*(1), 3–22. https://doi.org/10.1175/1520-0485(2004)034<0003:TNPCOW>2.0.CO;2

Sugimoto, S., & Hanawa, K. (2011). Roles of SST anomalies on the wintertime turbulent heat fluxes in the kuroshio-oyashio confluence region: Influences of warm eddies detached from the kuroshio extension. *Journal of Climate*, *24*(24), 6551–6561. https://doi.org/10.1175/2011JCLI4023.1

Sugimoto, S., Takahashi, N., & Hanawa, K. (2013). Marked freshening of North Pacific subtropical mode water in 2009 and 2010: Influence of freshwater supply in the 2008 warm season. *Geophysical Research Letters*, *40*(12), 3102–3105. https://doi.org/10.1002/grl.50600

Sugimoto, S., Kobayashi, N., & Hanawa, K. (2014). Quasi-decadal variation in intensity of the western part of the winter subarctic SST front in the Western North Pacific: The influence of Kuroshio extension path state. *Journal of Physical Oceanography*, *44*(10), 2753–2762. https://doi.org/10.1175/JPO-D-13-0265.1

Taguchi, B., Xie, S.-P., Schneider, N., Nonaka, M., Sasaki, H., & Sasai, Y. (2007). Decadal variability of the Kuroshio Extension: Observations and an eddy-resolving model hindcast. *Journal of Climate*, *20*(11), 2357–2377. https://doi.org/10.1175/JCLI4142.1

Taguchi, B., Qiu, B., Nonaka, M., Sasaki, H., Xie, S.-P., & Schneider, N. (2010). Decadal variability of the Kuroshio Extension: mesoscale eddies and recirculations. *Ocean Dynamics*, *60*(3), 673–691. https://doi.org/10.1007/s10236-010-0295-1

Taguchi, B., Nakamura, H., Nonaka, M., Komori, N., Kuwano-Yoshida, A., Takaya, K., & Goto, A. (2012). Seasonal evolutions of atmospheric response to decadal SST anomalies in the North Pacific subarctic frontal zone, observations and a coupled model simulation. *Journal of Climate*, *25*(1), 111–139. https://doi.org/10.1175/JCLI-D-11-00046.1

Tanimoto, Y., Nakamura, H., Kagimoto, T., & Yamane, S. (2003). An active role of extratropical sea surface temperature anomalies in determining anomalous turbulent heat flux. *Journal of Geophysical Research*, *108*(C10), 3304. https://doi.org/10.1029/2002JC001750

Tomita, H., Hihara, T., Kako, S., Kubota, M., & Kutsuwada, K. (2019). An introduction to J-OFURO3, a third-generation Japanese ocean flux data set using remote-sensing observations. *Journal of Oceanography*, *75*(2), 171–194. https://doi.org/10.1007/s10872-018-0493-x

Tsujino, H., Usui, N., & Nakano, H. (2006). Dynamics of Kuroshio path variations in a high-resolution general circulation model. *Journal of Geophysical Research*, *111*, C11001.

https://doi.org/10.1029/2005JC003118

Usui, N., Fujii, Y., Sakamoto, K., & Kamachi, M. (2015). Development of a four-dimensional variational assimilation system for coastal data assimilation around Japan. *Monthly Weather Review*, *143*(10), 3874–3892. https://doi.org/10.1175/MWR-D-14-00326.1

Usui, N., Wakamatsu, T., Tanaka, Y., Hirose, N., Toyoda, T., Nishikawa, S., et al. (2017). Four-dimensional variational ocean reanalysis: a 30-year high-resolution dataset in the western North Pacific (FORA-WNP30). *Journal of Oceanography*, *73*(2), 205–233. https://doi.org/10.1007/s10872-016-0398-5

Vialard, J., & Delecluse, P. (1998). An OGCM Study for the TOGA decade. Part I: Role of salinity in the physics of the Western Pacific fresh pool. *Journal of Physical Oceanography*, *28*(6), 1071–1088. https://doi.org/10.1175/1520-0485(1998)028<1071:AOSFTT>2.0.CO;2

Vivier, F., Kelly, K. A., & Thompson, L. A. (2002). Heat budget in the Kuroshio extension region: 1993-99. *Journal of Physical Oceanography*, *32*(12), 3436–3454. https://doi.org/10.1175/1520-0485(2002)032<3436:HBITKE>2.0.CO;2

Wagawa, T., Ito, S. I., Shimizu, Y., Kakehi, S., & Ambe, D. (2014). Currents associated with the quasi-stationary jet separated from the Kuroshio extension. *Journal of Physical Oceanography*, *44*(6), 1636–1653. https://doi.org/10.1175/JPO-D-12-0192.1

Yan, Y., Chassignet, E. P., Qi, Y., & Dewar, W. K. (2013). Freshening of subsurface waters in the northwest pacific subtropical gyre: Observations and dynamics. *Journal of Physical Oceanography*, *43*(12), 2733–2751. https://doi.org/10.1175/JPO-D-13-03.1

Yang, Y., San Liang, X., Qiu, B., & Chen, S. (2017). On the decadal variability of the eddy kinetic energy in the Kuroshio extension. *Journal of Physical Oceanography*, *47*(5), 1169–1187. https://doi.org/10.1175/JPO-D-16-0201.1

Yasuda, I. (2003). Hydrographic structure and variability in the Kuroshio-Oyashio Transition Area. *Journal of Oceanography*, *59*(4), 389–402. https://doi.org/https://doi.org/10.1023/A:1025580313836

Yasuda, T., & Hanawa, K. (1997). Decadal changes in the mode waters in the midlatitude North Pacific. *Journal of Physical Oceanography*. https://doi.org/10.1175/1520-0485(1997)027<0858:DCITMW>2.0.CO;2

Yuan, X., & Talley, L. D. (1996). The subarctic frontal zone in the North Pacific: Characteristics of frontal structure from climatological data and synoptic surveys. *Journal of Geophysical*

Research: Oceans, *101*(C7), 16491–16508. https://doi.org/10.1029/96JC01249

Zhang, Y., Du, Y., & Qu, T. (2016). A sea surface salinity dipole mode in the tropical Indian Ocean. *Climate Dynamics*, *47*(7–8), 2573–2585. https://doi.org/10.1007/s00382-016-2984-z

Zheng, F., & Zhang, R.-H. (2012). Effects of interannual salinity variability and freshwater flux forcing on the development of the 2007/08 La Niña event diagnosed from Argo and satellite data. *Dynamics of Atmospheres and Oceans*, *57*, 45–57. https://doi.org/10.1016/j.dynatmoce.2012.06.002

Zheng, F., & Zhang, R.-H. (2015). Interannually varying salinity effects on ENSO in the tropical Pacific: A diagnostic analysis from Argo. *Ocean Dynamics*, *65*(5), 691–705. https://doi.org/10.1007/s10236-015-0829-7

Zhu, J., Huang, B., Zhang, R.-H., Hu, Z.-Z., Kumar, A., Balmaseda, M. A., et al. (2015). Salinity anomaly as a trigger for ENSO events. *Scientific Reports*, *4*, 6821. https://doi.org/10.1038/srep06821